

¹ Susceptible host dynamics explain pathogen resilience to
² perturbations

⁴
⁵ Sang Woo Park,^{1,*} Sarah Cobey¹, Bjarke Frost Nielsen² Emily Howerton² Bryan T.
⁶ Grenfell^{2,3,4} Sarah Cobey¹

⁷ ¹ Department of Ecology and Evolution, University of Chicago, Chicago, IL, USA

⁸ ² Department of Ecology and Evolutionary Biology, Princeton University,
Princeton, NJ, USA

¹⁰ ³ High Meadows Environmental Institute, Princeton University, Princeton, NJ,
USA

¹² ⁴ Princeton School of Public and International Affairs, Princeton, NJ, USA

¹³ *Corresponding author: swp2@uchicago.edu

¹⁴ Abstract

¹⁵ Major priority for epidemiological research in the time of anthropogenic
¹⁶ change is understanding how infectious disease dynamics respond to perturbations.
¹⁷ Interventions to slow the spread of COVID-19 SARS-CoV-2 significantly disrupted
¹⁸ the transmission of other human pathogens, providing unique opportunities to learn
¹⁹ about pathogen characteristics from spatiotemporal variation in re-emergence patterns.
²⁰ As interventions lifted, a key question of whether and when respiratory pathogens
²¹ would eventually return to their pre-pandemic dynamics remains to be answered. To
²² address this gap, we develop Here, we present a framework for estimating pathogen
²³ resilience based on how fast epidemic patterns return to approach their pre-pandemic,
²⁴ endemic dynamics. Our analysis reveals a possibility and analyze relevant time series
²⁵ data from Hong Kong, Canada, Korea, and the US. By quantifying the resilience
²⁶ of common respiratory pathogens, we are able to predict when each pathogen will
²⁷ eventually return to pre-pandemic dynamics. Our predictions closely match the
²⁸ observed deviations (or lack thereof) from the pre-COVID dynamics of respiratory
²⁹ pathogens. Discrepancies between predicted and observed dynamics indicate the
³⁰ long-term impacts of pandemic perturbations, suggesting that some pathogens may
³¹ have settled to endemic cycles that are different from their pre-pandemic patterns be
³² converging to a different endemic cycle. Finally, we show that the replenishment rate
³³ of the susceptible pool is a key determinant of pathogen resilience. Our framework
³⁴ offers a novel perspective to characterizing the dynamics of endemic pathogens and
³⁵ their responses to COVID-19 interventions., which in turn determines the sensitivity
³⁶ of a system to stochastic perturbations. Overall, our analysis highlights the persistent
³⁷ nature of common respiratory pathogens compared to vaccine-preventable infections,
³⁸ such as measles.

39 Understanding how ecological systems respond to perturbations is a fundamental
40 challenge in predicting species persistence and extinction [1, 2, 3]. These responses
41 can be characterized in terms of resilience, which often measures how fast a system
42 returns to its stable, reference state following a perturbation [4, 5, 6, 7]. Both
43 theoretical and empirical efforts to quantify resilience of ecological systems have
44 provided key insights for understanding the dynamics of complex systems and linking
45 these findings to actionable strategies for species conservation [8]. However, despite
46 rich literature on ecological resilience, there have been limited applications to measuring
47 the resilience of host-pathogen systems, especially for human pathogens.

48 Introduction

49 Non-pharmaceutical interventions (NPIs) to slow the spread of COVID-19 SARS-CoV-2
50 disrupted the transmission of other human pathogens, providing large-scale natural
51 experiments for understanding how various host-pathogen systems respond to perturbations
52 [9, 10, 11, 12]. In particular, as respiratory pathogens, adding uncertainties to their
53 future epidemic dynamics and their public health burden [9]. As interventions
54 lifted, large heterogeneities in outbreak dynamics were observed across different
55 pathogens in different countries (Figure 1), likely reflecting differences in NPI, with
56 some pathogens exhibiting earlier and faster resurgences than others [10, 11, 12].
57 Heterogeneities in the overall reduction in transmission and the timing of re-emergence
58 likely reflect differences in intervention patterns, pathogen characteristics, immigration/
59 importation from other countries, and pre-pandemic pathogen dynamics [13]
60 –[14]. Therefore, comparing the differential impact of the pandemic perturbations
61 across pathogens can provide unique opportunities to learn about underlying pathogen
62 characteristics, such as their transmissibility or duration of immunity, from heterogeneities
63 in re-emergence patterns [13].

64 Even though more than four years have already five years have passed since the
65 emergence of COVID-19, current circulation patterns for many respiratory pathogens
66 appear to be different from their SARS-CoV-2, we still observe persistent changes in
67 pathogen dynamics following the pandemic perturbations. For example, compared
68 to pre-pandemic, seasonal patterns, especially in Hong Kong and Korea: some
69 pathogens, such as human metapneumovirus and bocavirus in Korea, are circulating
70 human metapneumovirus in Korea seems to circulate at lower levels, whereas other
71 pathogens, such as RSV in Korea, seem seems to exhibit different seasonality (Figure
72 1). These observations pose two fundamental questions for current and suggest
73 a possibility of a long-term change in pathogen dynamics following the pandemic
74 perturbations, which might be driven by a long-term shift in either human behavior
75 or population-level immunity [15, 16]. For example, the emergence of SARS-CoV-2
76 could have caused a long-term shift in population-level immunity through its interactions
77 with other pathogens [17], especially with seasonal coronaviruses [15, 18, 19]. The
78 possibility of a long-lasting impact of the pandemic perturbations poses an important

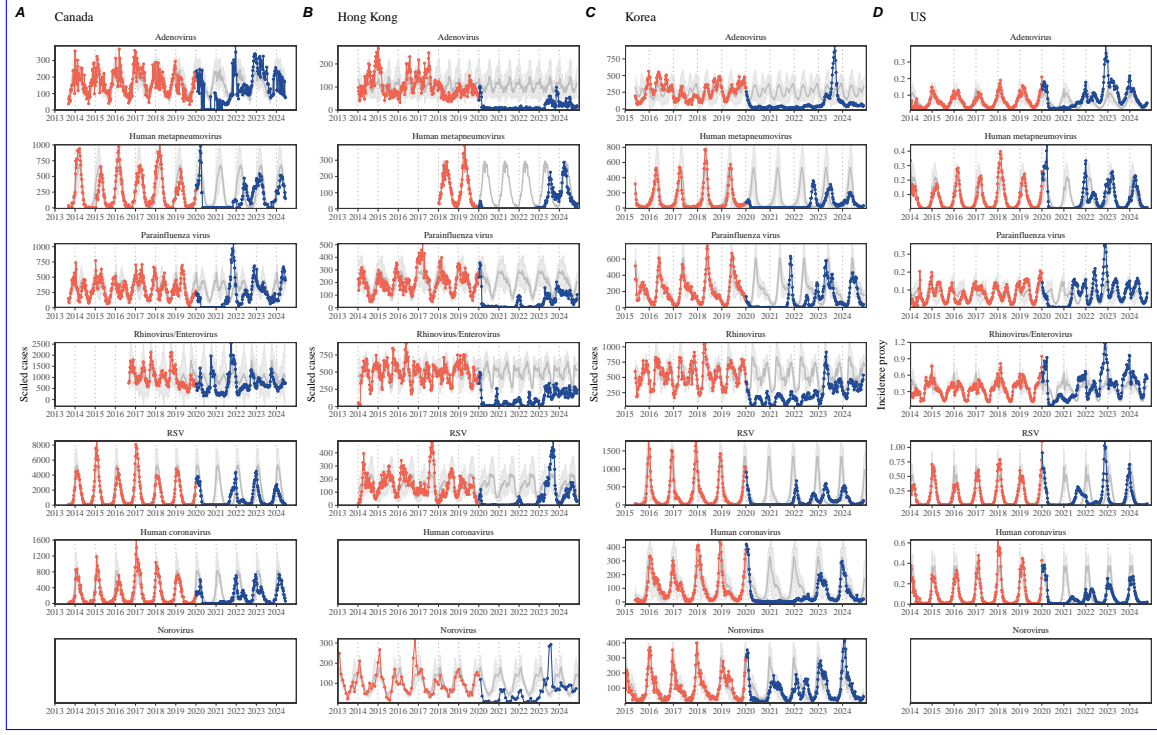


Figure 1: **Observed heterogeneity in responses to pandemic perturbations across respiratory pathogens and norovirus in (A) Canada, (B) Hong Kong, (C) Korea, and (D) US.** Red points and lines represent data before 2020. Blue points and lines represent data since 2020. Gray lines and shaded regions represent the mean seasonal patterns and corresponding 95% confidence intervals around the mean. Mean seasonal patterns were calculated by aggregating cases before 2020 into 52 weekly bins and taking the average in each week. Cases were scaled to account for changes in testing patterns (Materials and Methods).

79 question for future infectious disease dynamics: (1) can we learn about underlying
 80 pathogen characteristics, such as their transmissibility or duration of immunity, from
 81 re-emergence patterns? and (2) can we predict whether and when other
 82 respiratory pathogens will eventually return to their pre-pandemic dynamics?

83 **Observed heterogeneity in responses to COVID-19 pandemic across**
 84 **respiratory pathogens and norovirus in (A) Canada, (B) Hong Kong,**
 85 **(C) Korea, and (D) US.** Red points and lines represent data before 2020. Blue
 86 points and lines represent data since 2020. Gray lines and shaded regions represent
 87 the mean seasonal patterns and corresponding 95% confidence intervals based on
 88 the observed outbreak patterns before 2020. So far, most analyses of respiratory
 89 pathogens after pandemic perturbations have focused on characterizing the timing
 90 of rebound [9, 20, 14]. Instead, we seek to characterize how fast (and whether)
 91 a pathogen returns to its pre-pandemic dynamics. These two concepts have a
 92 subtle but important difference. For example, it took more than 3 years for human

metapneumovirus to rebound in Hong Kong, but the observed epidemic patterns in 2024 appear similar to pre-pandemic seasonal means, suggesting a possible return to pre-pandemic dynamics, though confirmation may require multiple seasons (Figure 1). Measuring this rate of return is useful because it allows us to quantify the ecological resilience of a host-pathogen system, which can inform responses to future interventions [4, 5, 6, 7].

To address this question, we propose a framework for In this study, we lay out theoretical and statistical approaches to characterizing the resilience of a host-pathogen system based on how fast the system recovers from perturbation. We begin by laying out a few representative scenarios that capture the potential impact of COVID-19 interventions pandemic perturbations on endemic pathogen dynamics and illustrating illustrate how resilience can be measured by comparing the pre- and post-pandemic dynamics of susceptible and infected hosts. In practice, information on susceptible hosts are is often unavailable, and traditional methods for reconstructing the dynamics of susceptible hosts require long-term endemic time series [21, 22], which cannot be applied due to disruptions in epidemic patterns caused by COVID-19 interventions making this theoretical approach infeasible. Instead, we utilize Takens' embedding theorem a mathematical technique to reconstruct empirical attractors from data and further measure the distance from this empirical attractor [23]. This reconstruction the data [23], which allows us to characterize measure the rate at which this distance decreases over time, which correspond to pathogen resilience. We apply this framework to analyzing the host-pathogen system approaches this empirical attractor after a perturbation; we define this rate to be the empirical resilience of the host-pathogen system. We use this method to analyze pathogen surveillance data for a wide array of respiratory and non-respiratory pathogens from Canada, Hong Kong, Korea, and the US. Finally, we show that susceptible host dynamics are a key determinants of pathogen resilience. Our study offers unique insights into understanding pathogen re-emergence patterns following COVID-19 interventions. explain variation in pathogen resilience and further demonstrate that more resilient pathogens will be less sensitive to perturbations caused by demographic stochasticity, thereby providing a direct link between pathogen resilience and persistence.

124

125 Conceptual introduction to pathogen resilience

In the classical ecological literature, the resilience of an ecological system is measured by the rate at which the system returns to its reference state following a perturbation [4, 5, 6, 7]. This rate corresponds to the largest real part of the eigenvalues of the linearized system near equilibrium—here, we refer to this value as the *intrinsic* resilience of the system, which represents the expected rate of return from perturbed states. However, respiratory pathogens often exhibit seasonal variation in transmission, meaning that In practice, we rarely know the true model describing population-level

133 dynamics of common respiratory pathogens, limiting our ability to infer the intrinsic
134 resilience of a host-pathogen system varies across season. Nonetheless system. Instead,
135 we can still measure the empirical resilience of a host-pathogen system by looking at
136 how fast the system returns to the pre-pandemic pre-perturbation, endemic dynamics
137 after interventions are lifted. the perturbation has ended. The COVID-19 pandemic
138 provides a particularly useful example of a major perturbation, providing unique
139 opportunities to measure the resilience of a host-pathogen system.

140 Resilience of a single-strain system under a short-term perturbation.

141 As an example, consider an intervention that reduce we begin with a simple Susceptible-Infected-Recover
142 (SIRS) model with seasonally forced transmission and demography (i.e., birth and
143 death). The SIRS model is the simplest model that allows for the waning of immunity
144 and is commonly used for modeling the dynamics of respiratory pathogens [24]. First,
145 consider a pandemic perturbation that reduces transmission by 50% for 6 months
146 starting in 2020, which causes epidemic patterns to deviate from its their original
147 stable annual cycle for a short period of time and eventually come back (Figure 2A).
148 To measure the empirical resilience of this system empirically, we first need to be able
149 to measure the distance from its pre-pandemic attractor, which is defined as a set of
150 points in state space or phase plane that the system is pulled towards [25]. There are
151 many different ways we can measure the distance from the attractor, but for illus-
152 trative purposes, we choose one of the most parsimonious approachapproaches: that
153 is, we look at how the susceptible (S) and infected (I) populations change over time
154 and measure the Euclidean distance on the SI phase plane, using the counterfactual
155 unperturbed phase plane as a reference (Figure 2B; Materials and Methods). In this
156 simple case, the locally estimated scatterplot smoothing (LOESS) fit indicates that
157 the distance from attractor decreases linearly on the attractor decreases exponentially
158 (linearly on a log scale) on average (Figure 2C). Furthermore, the overall rate of re-
159 turn matches approximates the intrinsic resilience of the seasonally unforced system
160 (Figure 2C).

161 Alternatively, NPIs can permanently change our behavior and have persisting

162 Resilience of a single-strain system under a long-term perturbation. Alternatively,
163 pandemic perturbations can have a lasting impact on the pathogen dynamics; as
164 forces driving pathogen dynamics through a long-term reduction in transmission or
165 permanent change in immunity. As an example, we consider a scenario in which a
166 10% reduction in transmission persists even after the NPIs major pandemic perturbations
167 are lifted (Figure 2D–F). In such cases, we cannot know whether the pathogen will
168 return to its original cycle or a different cycle until many years have passed after the
169 NPIs are lifted, meaning that, and we cannot measure the distance against the new to
170 the new unknown attractor that the system will might eventually approach. Nonethe-
171 less, we can still measure the distance against the original, from the pre-pandemic
172 attractor and ask how the distance changes over time (Figure 2E). The LOESS fit
173 suggests that the distance from the pre-pandemic attractor will initially decrease ex-
174ponentially on average (equivalently, linearly on a log scale) and eventually plateau
175 (Figure 2F). Here, a permanent 10% reduction in transmission rate slows down the

176 system, which causes the distance from the ~~attractor~~ pre-pandemic attractor initially
177 to decrease at a slower rate (Figure 2F) than it would have otherwise ~~in the absence of~~
178 ~~permanent transmission reduction~~ (Figure 2C) ~~before plateauing at a fixed distance~~
179 ~~between the two attractors~~. This example shows that resilience is not necessarily an
180 intrinsic property of a specific pathogen. Instead, pathogen resilience is a property
181 of a specific attractor that a host-pathogen system approaches, which depends on
182 both pathogen and host characteristics.

183 **Resilience of a single-strain system with long-term transients.** Finally,
184 transient phenomena can ~~also further~~ complicate the picture (Figure 2G–I). For ex-
185 ample, a stage-structured model ~~for RSV~~, which accounts for reduction in secondary
186 susceptibility, initially exhibits a stable annual cycle, but perturbations from ~~NPIs~~
187 ~~a 10% reduction in transmission for 6 months~~ cause the epidemic to ~~exhibit shift~~ to
188 biennial cycles (Figure 2G). ~~Despite this biennial cycle, we see that the~~ The system
189 eventually approaches the original pre-pandemic attractor (Figure 2H), suggesting
190 that this biennial cycle is a transient ~~phenomenon~~. The LOESS fit indicates that the
191 distance from the attractor ~~will initially decrease~~ ~~initially decreases~~ exponentially
192 at a rate that is consistent with the intrinsic resilience of the seasonally unforced
193 ~~stage-structured~~ system, but the ~~rate of decrease slows down as the epidemic exhibits~~
194 ~~a biennial cycle approach to the attractor slows down with the damped oscillations~~
195 (Figure 2I). ~~In classical ecological theory, this~~ This behavior is also referred to as a
196 ghost attractor, which causes long transient dynamics and slow transitions [26]. As
197 we show in Supplementary Figure S1, strong ~~Strong~~ seasonal forcing in transmission
198 can also lead to transient phenomena for a simple SIRS model, causing a ~~slowing~~
199 ~~down of the system~~ slow return to pre-perturbation dynamics (Supplementary Figure
200 S1).

201 In Supplementary Materials, we also explore measuring **Resilience of a two-strain**
202 **system.** This empirical approach allows us to measure the resilience of a two-
203 strain host-pathogen system : ~~when the dynamics~~ ~~two strains (or two pathogens)~~ are
204 ~~coupled through cross immunity, we would expect the entire system to be characterized~~
205 ~~by a single resilience value (rather than having two separate resilience for each~~
206 ~~strain)~~ as well even when we have incomplete observation of the infection dynamics.
207 Simulations from a simple two-strain competition system illustrate that separate
208 analyses of individual strain dynamics (e.g., RSV A vs B) and a joint analysis of total
209 infections (e.g., total RSV infections) yield identical resilience estimates , confirming
210 our expectation (Supplementary Figure S2, 3). This is expected because eigenvalues
211 determine the dynamics of the entire system around the equilibrium, meaning that
212 both strains should exhibit identical rates of return following a perturbation. Analogous
213 to a ~~single~~ single-strain system, strong seasonal forcing in transmission can cause
214 the ~~two-strain~~ system to slow down through transient phenomena (Supplementary
215 Figure S4).

216 These observations indicate three possibilities yield three insights. First, we can
217 directly estimate the empirical resilience of a host-pathogen system by looking at how
218 fast measuring the rate at which the system approaches a pre-pandemic an attractor,

219 provided that we ~~can measure~~ have a way to quantify the distance from ~~attractor~~^{the} attractor—as we discuss later, the attractor of a system can be reconstructed from
220 ~~data from mathematical theory without making assumptions about the underlying~~^{the} model. The empirical approach to estimating pathogen resilience is particularly convenient because it does not require us to know the true underlying model. ~~As we show~~
221 ~~in Supplementary Figure S5,;~~ estimating the intrinsic resilience from fitting ~~standard~~
222 ~~compartimental misspecified~~ models can lead to biased estimates ~~, especially under~~
223 ~~model misspecification~~(^{Supplementary Figure S5}). Second, resilience estimates allow us to make phenomenological predictions about the dynamics of a host-pathogen system following a perturbation: ~~assuming that~~. ~~Assuming that an attractor has not~~
224 ~~changed and~~ the distance from the attractor will decrease exponentially over time, we can ~~obtain a ballpark estimate for~~ estimate when the system ~~will~~ ~~should~~ reach
225 an attractor. Finally, ~~deviation from an exponential decrease in the distance from~~
226 ~~attractor can~~ a change in the (exponential) rate of approach provide information
227 about whether the system has reached an alternative attractor, or a ghost attractor, that is different from the original, pre-pandemic attractor. These alternative attractors may reflect ~~continued perturbations from~~ permanent changes in transmission patterns as well as changes in immune landscapes. ~~There will be periods of~~
228 ~~time when it is difficult to tell whether pathogen dynamics are still diverging from~~
229 ~~the original attractor due to a long-term perturbation, or have entered the basin~~
230 ~~of attraction of a new attractor.~~ Now that several years have passed since major interventions have been lifted, many respiratory pathogens may have had sufficient time to begin returning to their post-intervention attractors—empirical comparisons between current cases and pre-pandemic cases are consistent with this hypothesis (Figure 1). With recent data, we can start to evaluate whether we see early signs of convergence to the former attractor or a new one.

245 Inferring pathogen resilience from real data

246 Based on these ~~observations~~^{patterns}, we now ~~set out to infer pathogen resilience from~~
247 ~~real data.~~ Here, we briefly lay out our approach to estimating pathogen resilience from real data (Figure 3). We ~~then test~~ first tested this approach against simulations and ~~apply~~ applied it to real data. Specifically, we analyzed case time series of
248 ~~respiratory pathogens from four countries: Canada, Hong Kong, Korea, and the US.~~
249

250 So far, we ~~have~~ focused on simple examples that assume a constant transmission reduction ~~during the pandemic~~. However, in practice, the impact of ~~NPIs~~
251 ~~pandemic perturbations~~ on pathogen transmission ~~is~~^{was} likely more complex (Figure 3A), reflecting introduction and relaxation of various intervention strategies. ~~These~~
252 ~~complexities can~~ In some cases, strong perturbations likely caused local fadeouts, requiring immigration/importation from another location for epidemic rebound. Such
253 ~~complexities could~~ lead to longer delays between the introduction of ~~NPIs~~ and pathogen

259 ~~re-emergence~~ pandemic perturbations and pathogen rebound as well as temporal
260 variation in outbreak sizes (Figure 3B); in this example, continued transmission
261 reduction from ~~NPIs~~ interventions limits the size of the first outbreak in 2021 follow-
262 ing the ~~emergence~~ rebound, allowing for a larger outbreak in 2022 when ~~NPIs~~
263 interventions are further relaxed.

264 Previously, we relied on the dynamics of susceptible and infected hosts to com-
265 pute the distance from ~~the~~ attractor (Figure 2), but information on susceptible
266 hosts ~~are often not~~ ~~is rarely~~ available in practice. In addition, uncertainties in case
267 counts due to observation error ~~as well as the possibility of complex, multiannual~~
268 ~~attractor adds challenges to measuring, strain evolution, and multiannual cycles in~~
269 ~~the observed epidemic dynamics (e.g., adenovirus circulation patterns in Hong Kong~~
270 ~~and Korea) add challenges to defining pre-pandemic attractors, which limits our~~
271 ~~ability to measure~~ the distance from ~~the~~ attractor. To address these challenges, we
272 ~~first can~~ reconstruct an empirical attractor by utilizing Takens' theorem [23], which
273 states that an attractor of a nonlinear multidimensional system can be mapped onto
274 a delayed embedding [23]. Here, we use delayed copies of (Materials and Methods).
275 For example, we can use delayed logged values of pre-pandemic cases $C(t)$ (Figure
276 3C) to reconstruct the attractor:

$$\langle \log(C(t) + 1), \log(C(t - \tau) + 1), \dots, \log(C(t - (M - 1)\tau) + 1) \rangle, \quad (1)$$

277 where the delay τ and embedding dimension M are determined based on autocorre-
278 lations and false nearest neighbors, respectively [27, 28]. We This allows us to define
279 the pre-pandemic attractor as a points on an M dimensional space. We can then
280 apply the same delay and embedding dimensions to the entire time series to deter-
281 mine the position ~~on a in~~ multi-dimensional state space (Figure 3D), which allows
282 us to measure the nearest neighbor distance between the current state of the sys-
283 tem and the empirical pre-pandemic attractor (Figure 3E). In principle Specifically,
284 the nearest neighbor distance is calculated by computing the distance between the
285 current position on the M dimensional space and all points in the empirical attractor
286 set and taking the minimum value. In theory, we can now quantify how fast this
287 distance decreases by fitting a linear regression on a log scale, where the slope of the
288 linear regression corresponds to pathogen resilience. As we show in Supplementary
289 Figure S6, overall temporal variations in the distance from attractor, especially the
290 observed rate of decrease, appear robust empirically measures pathogen resilience
291 with a steeper slope corresponding to a higher resilience estimate (Figure 3E). However,
292 resulting estimates of pathogen resilience can be sensitive to choices about embed-
293 ding delays and dimensions; we note that. For example, using longer delays and
294 higher dimensions ~~tend~~ tends to smooth out temporal variations in the distance from
295 attractor the attractor (Supplementary Figure S6).

296 Complex changes in the distance from ~~the~~ attractor suggest that estimating
297 pathogen resilience from linear regression will likely be be particularly sensitive to
298 our choice of fitting windows for the regression . In Supplementary Materials, we
299 explore (Figure 3E). Therefore, before we tried estimating resilience from real data,

300 we explored an automated window selection criterion for linear regression and
301 test tested it against randomized, stochastic simulations across a wide range of real-
302 istic NPI shapes. We find that resilience estimates based on the automated window
303 selection criteria are moderately correlated (0.48) with the pandemic perturbation
304 shapes. In doing so, we also explored optimal choices for embedding dimensions
305 and evaluated our choices of fitting window parameters and embedding dimensions
306 by quantifying correlation coefficients between the estimated resilience and the in-
307trinsic resilience of the post-NPI attractor (a seasonally unforced system (Materials
308 and Methods). Overall, we found large variation in estimation performances with
309 correlation coefficient ranging from 0.21 to 0.61 (Supplementary Figure S7). In
310 contrast, almost all cases, the automated window selection approach outperformed
311 a naive approach that uses the entire time series, starting from , which performs
312 regression between the peak distance , only gives a correlation of 0.09 and consistently
313 underestimates the intrinsic resilience and current distance (Supplementary Figure
314 S7).

315 Now, we apply Based on the best performing window selection criteria and
316 embedding dimension, we applied this approach to pathogen surveillance data pre-
317 sented in Figure 4 (Materials and Methods). For each time series, we apply applied
318 Takens' theorem independently to reconstruct the empirical attractor and obtain
319 obtained the corresponding time series of distance distances from attractors (Sup-
320 plementary Figure S8for the distance time series and linear regression fits). Then, we
321 use used the automated window selection criterion to fit a linear regression
322 and estimate estimated the empirical resilience for each pathogen in each country
323 . For most respiratory pathogens (Supplementary Figure S8); the window selection
324 criterion gave poor regression window for three cases (norovirus in Hong Kong and
325 Korea and rhinovirus/enterovirus in the US), leading to unrealistically low resilience
326 estimates, and so we used ad-hoc regression windows instead (Supplementary Figure
327 S9; Materials and Methods).

328 For all pathogens we considered, resilience estimates fall fell between 0.4/year and
329 1.8/year (Figure 4A), with the exception of Rhinovirus in the US (0.066/year; 95%
330 CI: 0.018/year–0.113/year) and Bocavirus in Korea (0.087/year; 95% CI: 0.023/year–0.151/year).
331 Excluding these exceptions, . We estimated the mean resilience of common res-
332piratory pathogens is 0.974/year to be 0.99/year (95% CI: 0.784/year–0.81/year–
333 1.16/year). As a 1.18/year. For reference, this is ≈7 ≈ 7.5 times higher than
334 the intrinsic resilience of pre-vaccination measles dynamics in England and Wales
335 (≈ 0.13/year). Finally, resilience estimates for norovirus appears to be comparable
336 to the intrinsic resilience of measles: 0.119/year , a gastrointestinal pathogen, were
337 comparable to those of common respiratory pathogens: 1.44/year (95% CI: 0.004/year–1.01/year–
338 0.233/year) for Korea and 0.385/year 1.87/year for Hong Kong and 1.07/year (95%
339 CI: 0.167/year–0.86/year–0.603/year) . A simple ANOVA shows that there are 1.29/year
340 for Korea. Based on a simple ANOVA test, we did not find significant differences in
341 resilience estimates across countries ($p < 0.036$) and pathogens ($p < 0.030$, $p = 0.25$)
342 or pathogens ($p = 0.67$).

343 Using resilience estimates, we now predict predicted when each pathogen will
344 would hypothetically return to their original pre-pandemic cycles dynamics, assuming
345 no long-term change in the attractor. Specifically, we extend extended our linear
346 regression fits to distance-from-attractor time series and ask when the predicted re-
347 gression line will cross a threshold value, which we set to a; since we relied on nearest
348 neighbor distances, pre-pandemic distances are always greater than zero (Figure 3E),
349 meaning that we can use the mean of pre-pandemic distances. We predict as our
350 threshold.

351 We predicted that a return to pre-pandemic cycles has occurred or would be immin-
352 ent for most pathogens (Figure 4B; see Supplementary Figure S9 for a zoomed out
353 version). In addition, we also predict that many pathogens particular, we predicted
354 that 12 out of 23 pathogen-country pairs should have already returned to their
355 pre-pandemic dynamics by before the end of 2024. For almost all pathogens that were
356 predicted to have returned already, the observed epidemic dynamics showed clear
357 convergence towards their pre-pandemic seasonal averages, confirming our predictions
358 (Figure 4C). However, there were a few exceptions, including norovirus in Hong Kong
359 and rhinovirus/enterovirus in the US, where the observed epidemic dynamics in 2024
360 ; but these predictions contradict some of the observed pathogen dynamics. For
361 example, we predict that both human metapneumovirus and RSV in Korea should
362 have returned to their attractors by now, but the magnitude and timing of recent
363 epidemics are different from exhibit clear deviation from their pre-pandemic patterns
364 (Figure 4C; Figure S9). These observations suggest the a possibility that some common respiratory pathogens may have converged to different
365 attractors.

367 In Supplementary Materials, we also consider using a lower threshold for the
368 false nearest neighbor approach when determining the embedding dimension; this
369 gives a higher embedding dimension. As explained earlier (Supplementary Figure
370 S6), this gives a smoother distance-from-attractor time series (compare or are still
371 exhibiting non-equilibrium dynamics. In contrast, pathogens that were predicted to
372 have not returned yet also showed clear differences from their pre-pandemic seasonal
373 averages; as many of these pathogens are predicted to return in 2025–2026, we may
374 be able to test these predictions in near future (Supplementary Figure S10with S8);
375 this also requires us to use longer time series, which prevents us from estimating
376 resilience for some pathogens. Overall, resulting). Our reconstructions of distance
377 time series and estimates of pathogen resilience with higher embedding dimensions
378 still fall between 0.3/year and 2.1/year for the most part and expected return time
379 were generally robust to choices of embedding dimensions (Supplementary Figure
380 S11). A direct comparison between two approaches (i.e., original estimate vs using
381 higher dimensions) shows a strong consistency in resilience estimates (Supplementary
382 Figure S12). S11–12).

383 **Susceptible host dynamics explain variation in pathogen
384 resilience**

385 So far, we have focused on quantifying pathogen resilience from the observed patterns
386 of pathogen re-emergence following COVID-19 interventionspandemic perturbations.
387 But what factors determine how resilient a host-pathogen system is? Here, we use a
388 standard Susceptible-Infected-Recovered-Susceptible (SIRS) model to show that To
389 address this question, we used the SIRS model to explore how changes in susceptible
390 host dynamics are the key determinants of affect pathogen resilience. To do so, we
391 vary-varied the basic reproduction number \mathcal{R}_0 , which represents the average number
392 of secondary infections caused by a newly infected individual in a fully susceptible
393 population, and the duration of immunity and ecompute-computed intrinsic resilience
394 for each parameter.

395 We find-found that an increase in \mathcal{R}_0 and a decrease in the duration of immunity
396 correspond to an increase in pathogen resilience (Figure 5A). These variations
397 can be understood in terms of the susceptible host dynamics, where Similarly, an
398 increase in \mathcal{R}_0 and a decrease in the duration of immunity corresponds to a faster per-
399 capita susceptible replenishment rate causes the system to be more resilient (Figure
400 5B). This rate can be expressed as a rate of susceptible replenishment, which is
401 defined as the ratio between absolute rate at which new susceptibles enter the pop-
402 ulation and the equilibrium number of susceptible individuals in the population, \bar{S} .
403 Therefore, both S^* (Figure 5B). We note that a higher \mathcal{R}_0 and shorter duration of
404 immunity can drive drives a faster per-capita susceptible replenishment rate (Figure
405 5B), especially because higher \mathcal{R}_0 leads to lower \bar{S} by decreasing the susceptible
406 proportion at equilibrium S^* . For a simple SIR model that assumes a life-long
407 immunity, we can show analytically that pathogen resilience is proportional to the
408 per-capita rate of susceptible replenishment (Materials and Methods). Overall, these
409 observations suggest that a faster per-capita susceptible replenishment rate causes
410 the system to be more resilient.

411 Finally, we can now rank different pathogens based on By taking the average
412 values of empirical resilience , which allows us to determine values for each pathogen,
413 we were able to map each pathogen onto a set of parameters of the SIRS model
414 that are consistent with the estimated resilience corresponding resilience estimates
415 (Figure 5A). Across all pathogens we consider, except for boecavirus and norovirus,
416 we estimate-considered, we estimated that the average duration of immunity is likely
417 to be short ($< 6 < 4$ years) across a plausible range of \mathcal{R}_0 . These rankings further
418 allow us to map each pathogen onto a set of parameters that are consistent with its
419 empirical resilience (Figure 5A) and (< 6). We were also able to obtain a plausible
420 range of susceptible replenishment rates for each pathogen (Figure 5B). However,
421 we note that there is no, but there was a large uncertainty in the estimates for
422 susceptible replenishment rates due to a lack of one-to-one correspondence between
423 susceptible replenishment rates and pathogen resilience, leading to a wide uncertainty
424 in the estimates for susceptible replenishment rates (Figure 5B).

425 Pathogen resilience determines sensitivity to stochastic 426 perturbations

427 Even in the absence of major pandemic perturbations, host-pathogen systems are
428 expected to experience continued perturbations of varying degrees from changes in
429 epidemiological conditions, such as human behavior, climate, and viral evolution.
430 These perturbations can also arise from demographic stochasticity, which is inherent
431 to any ecological systems. Here, we used a seasonally unforced SIRS model with
432 constant birth and death rates to explore how resilience of a host-pathogen system
433 determines the sensitivity to perturbations caused by demographic stochasticity
434 (Materials and Methods).

435 We found that resilience of a host-pathogen system determines the amount of
436 deviation from the deterministic trajectory caused by demographic stochasticity,
437 with less resilient systems experiencing larger deviations (Figure 6). Notably, less
438 resilient systems also exhibited slower epidemic cycles (Figure 6A–C). The periodicity
439 of this epidemic cycle matched those predicted by the intrinsic periodicity of the
440 system (Supplementary Figure S13) where the intrinsic resilience of the system
441 is inversely proportional to its intrinsic periodicity (Supplementary Figure S14).
442 However, we note that the interplay between seasonal transmission and intrinsic
443 periodicity can also lead to complex cycles, as illustrated by a recent analysis of
444 *Mycoplasma pneumoniae* dynamics [29].

445 We also note that the intrinsic resilience is not the sole determinant for how
446 sensitive the system is to stochastic perturbations. For example, the population
447 size and average duration of infection also affect the amount of deviation from
448 the deterministic trajectory caused by demographic stochasticity, even though these
449 quantities have little to no impact on the intrinsic resilience (Supplementary Figure
450 S15). These conclusions were robust for the seasonally forced SIRS model (Supplementary
451 Figure S16).

452 Discussion

453 The COVID-19 interventions have pandemic interventions caused major disruptions
454 to circulation patterns of both respiratory and non-respiratory pathogens, adding
455 challenges to predicting their future dynamics [9, 10, 11, 12]. On the other hand, these
456 interventions However, these perturbations offer large-scale natural experiments for
457 understanding how different pathogens respond to perturbations. In this study, we
458 show showed that pathogen re-emergence patterns following COVID-19 interventions
459 pandemic perturbations can be characterized through the lens of ecological resilience. Traditionally, ecological resilience measures how fast a system returns to a reference
460 state following a perturbation. In the context of respiratory pathogens, resilience
461 measures how fast epidemics return to their endemic cycles after interventions are
462 lifted.

464 We use an attractor reconstruction approach to quantify how distance from
465 attractor changes over time for each pathogen [23]. We show that the resilience of a
466 and presented a new method for estimating pathogen resilience from time series data.
467 We showed that variation in pathogen resilience can be explained by the differences
468 in susceptible host dynamics, where faster replenishment of the susceptible pool
469 corresponds to a more resilient host-pathogen system can be estimated by fitting a
470 linear regression to a logged distance-from-attractor time series system. Finally,
471 we showed that pathogen resilience also determines the sensitivity to stochastic
472 perturbations.

473 We analyzed case time series of common respiratory infections and norovirus
474 infections from Canada, Hong Kong, Korea, and the US to estimate their resilience.
475 Overall, we estimate that the resilience for most common respiratory pathogens
476 ranges between estimated the resilience of these pathogens to range from 0.4/year
477 and to 1.8/year, which is 3–14 times more resilient than prevaccination measles;
478 . Consistent with other epidemiological evidence [30, 31, 32, 33], these resilience
479 estimates indicate that common respiratory pathogens and norovirus likely exhibit
480 faster susceptible replenishment and are therefore more persistent, indicating potential
481 challenges in controlling common respiratory these pathogens.

482 Our framework allows us to make Based on our resilience estimates, we made
483 phenomenological predictions about when each pathogen will return to their endemic
484 cycles. The ability to predict future epidemic patterns from resilience estimates offers
485 a new paradigm for epidemic forecasting. While this approach cannot predict the
486 exact timing of outbreaks or epidemic patterns, it is nonetheless useful for predicting
487 when epidemics will settle down to regular cycles after a large perturbation, such as
488 COVID-19 interventions.

489 Our analyses suggest a possibility that several pathogens may have converged
490 to different endemic cycles compared to their pre-pandemic epidemic patterns. Key
491 examples include human metapneumovirus, RSV, and bocavirus in Korea as well as
492 RSV in Hong Kong. For the most part, we accurately predicted which pathogens
493 should have already returned before the end of 2024. However, there were two
494 main exceptions (i.e., norovirus in Hong Kong and rhinovirus/enterovirus in the
495 US), suggesting that these pathogens may be converging to new endemic cycles
496 or experiencing long-term transient behavior. These changes may reflect changes in
497 surveillance or actual shift in the dynamics, caused by permanent changes in behavior
498 or population-level immunity. While it seems may seem unlikely that permanent
499 changes in behavior would only affect a few pathogens and not others, we cannot
500 rule out this possibility given heterogeneity in the age of infection across different
501 respiratory pathogens. A shift in population-level immunity is plausible, as the
502 emergence of SARS-CoV-2 and extinction of influenza B/Yamagata likely caused
503 major changes in immune landscapes; interactions among co-circulating pathogens,
504 such as cross immunity between RSV and HMPV [34], may have also contributed
505 to changes in population-level immunity. However, we currently do not know how
506 immunity, or lack thereof, from these pathogens would affect infection from other

507 pathogens. Future studies should use detailed mechanistic models, coupled with
508 behavioral and immunological data, to test these hypotheses and better understand
509 post-pandemic dynamics of endemic pathogens. differences in the observed mean
510 age of infections and therefore the differences in age groups that primarily drive
511 transmission [35, 36]. Differences in the mode of transmission between respiratory
512 vs gastrointestinal pathogens may also contribute to the differences in responses to
513 pandemic perturbations.

514 For almost half of the pathogens we considered, we predicted that their return
515 to original epidemic patterns is imminent. We will need a few more years of data
516 to test whether these pathogens will eventually return to their original dynamics or
517 eventually converge to a different attractor. We also cannot rule out the possibility
518 that some pathogens may exhibit long-term transient behaviors following pandemic
519 perturbations. Overall, these observations echo earlier studies that highlighted the
520 long-lasting impact of pandemic perturbations [16, 37, 38, 12, 29].

521 We show that susceptible host dynamics shape pathogen resilience, where
522 faster replenishment of the susceptible population causes the pathogen to be more
523 resilient. For simplicity, we focus on waning immunity and birth as a main
524 driver of the susceptible host dynamics but other mechanisms can
525 also contribute to the replenishment of the susceptible population. In particular,
526 pathogen evolution, especially the emergence of antigenically novel strains, can cause
527 effective waning of immunity in the population; therefore, we hypothesize that faster
528 rates of antigenic evolution can also cause a pathogen to be more resilient is
529 likely a key feature of pathogen resilience. Future studies should explore the relationship
530 between the rate of evolution and resilience for antigenically evolving pathogens.
531 This result also highlights the importance of detailed measurements of changes in
532 the susceptible population through serological assays for understanding pathogen
533 dynamics [39].

534 Quantifying pathogen resilience also offers novel approaches to validating population-
535 level epidemiological models. So far, the majority of most model validation in
536 epidemiology-infectious disease ecology is based on the ability of a model to reproduce
537 the observed epidemic dynamics and to predict future dynamics [40, 34, 32, 41, 42].
538 However, there can be plethora of models that meet many models can perform
539 similarly under these criteria. For example, two major RSV models have been pro-
540 posed so far to explain biennial epidemic patterns: (1) a stage- and age-structured
541 model that allows for disease severity to vary with number of past infections and age
542 of infection [32] and (2) a pathogen-interaction model that accounts for cross immu-
543 nity between RSV and human metapneumovirus-metapneumovirus [34]. Since both
544 models can accurately reproduce the observed epidemic patterns, standard criteria
545 for model validation do not allow us to distinguish between these two models from
546 population-level data alone. Instead, we can it would be possible to measure the
547 empirical resilience of each model by simulating various perturbations and compare
548 them-comparing the simulations to estimates of empirical resilience from data, using
549 COVID-19 interventions as an opportunity. Future studies should further investigate

550 ~~using pathogen resilience for validating epidemic models.~~ pandemic perturbations as
551 a reference.

552 There are several limitations to our work. First ~~of all~~, we did not extensively
553 explore other approaches to reconstructing the attractor. Recent studies showed
554 that more sophisticated approaches, such as using non-uniform embedding, can
555 provide more robust reconstruction for noisy data [28]. In the context of causal
556 inference, choices about embedding can have major impact on the resulting inference
557 [43]. Our resilience estimates are likely overly confident given a lack of un-
558 certainties in attractor reconstruction as well as the simplicity of our statistical
559 framework. ~~Short pre-pandemic time series also contributes to the crudeness of~~
560 ~~our estimates.~~ Nonetheless, as illustrated in our sensitivity analyses (Supplementary
561 Figure S6, S10–S12), inferences about pathogen resilience in our SIRS model ap-
562 pear to be robust to decisions about embedding lags and dimensions—this is be-
563 cause tracking the rate at which the system approaches the attractor is likely a
564 much simpler problem than making inferences about causal directionality. ~~Our~~
565 ~~Short pre-pandemic time series also limit our ability to accurately reconstruct the~~
566 ~~attractor and contribute to the crudeness of our resilience estimates; although this~~
567 ~~is less likely a problem for respiratory pathogens that are strongly annual, our~~
568 ~~attractor reconstruction may be inaccurate for those exhibiting multi-annual cycles,~~
569 ~~such as adenovirus in Hong Kong and Korea. Our framework also do not allow us~~
570 ~~to distinguish whether a system has settled to a new attractor or is experiencing~~
571 ~~long-term transient behavior. Uncertainties in pathogen dynamics due to changes in~~
572 ~~testing patterns further contribute to the crudeness of our resilience estimates.~~

573 While attractor reconstruction methods allow us to make model-free inferences
574 of pathogen resilience, it does not allow us to tease apart how different mechanisms
575 contribute to the resilience a host-pathogen system. Using the simple SIRS model,
576 we illustrated that susceptible host dynamics are key determinants for pathogen
577 resilience, but we also found that there isn't a one-to-one correspondence between
578 per capita replenishment rate of the susceptible population and pathogen resilience
579 estimates. Future studies should explore using mechanistic models to explain heterogeneity
580 in resilience estimates across different pathogens.

581 Finally, our simulation-based analyses primarily focused on single-strain systems
582 but real-world pathogens can interact with other pathogens, which can result in
583 complex dynamics [44, 45]. To address this limitation, we considered a simple
584 two-strain competition system with cross immunity and showed that the resilience
585 of a coupled system can be measured by studying the dynamics of either strains.
586 However, this conclusion likely depend on the strength of strain interaction as well as
587 the underlying details of the model. For example, ecological interference between two
588 unrelated pathogens [44] will likely generate weaker coupling than cross immunity
589 between related pathogens; in the former case, we do not necessarily expect two
590 unrelated pathogens to have same resilience despite their ecological interference.
591 Some pathogen strains can also exhibit positive interactions where infection by
592 one strain can lead to an increased transmission of another competing strain. For

example, previous studies showed that an increased dengue transmission through antibody-dependent enhancement can permit coexistence and persistence of competing strains [46]; based on these observations, we tentatively hypothesize that positive interactions such as antibody-dependent enhancement may increase the resilience of a system. Future studies should explore how different mechanisms of pathogen interactions contribute to the resilience of each competing pathogen as well as the entire system. Despite these limitations, our study illustrates that quantifying pathogen resilience can provide novel insights into pathogen dynamics. Furthermore, our qualitative prediction that common respiratory pathogens are more resilient than prevaccination measles is also likely to be robust ~~to these predictions~~, given how ~~rapid~~rapidly many respiratory pathogens returned to their original cycles following COVID-19 interventions, ~~pandemic perturbations~~.

Predicting the impact of anthropogenic changes on infectious disease dynamics is a fundamental aim of infectious disease research in a rapidly changing world. Our study illustrates that ~~quantifying pathogen resilience can help us understand how infectious disease pathogens respond to major perturbations caused by public health interventions~~ how a host-pathogen system responds to both small and large perturbations is largely predictable through the lens of ecological resilience. In particular, quantifying the resilience of a host-pathogen system offers a unique insight into questions about endemic pathogens' responses to pandemic perturbations, including whether some pathogens will exhibit long-lasting impact from the pandemic perturbation or not. More broadly, a detailed understanding of the determinants of pathogen resilience ~~may offer unique insights into pathogen persistence and controllability~~ can provide deeper understanding of pathogen persistence.

Materials and Methods

Data

We gathered time series on respiratory infections from ~~four different countries~~: Canada, Hong Kong, Korea, and United States (US). As a reference, we also included time series data on norovirus infections ~~for available countries—in when available~~. In contrast to respiratory pathogens, we ~~expect hypothesized~~ gastrointestinal viruses, such as norovirus, to be ~~less affected by COVID-19 intervention measures—differently affected by pandemic perturbations~~.

Weekly time series of respiratory infection cases in Canada came from a publicly available website by the Respiratory Virus Detection Surveillance System, which collects data from select laboratories across Canada [47]. Weekly time series of respiratory infection cases in Hong Kong came from a publicly available website by the Centre for Health Protection, Department of Health [48, 49]. Weekly time series of acute respiratory infection cases in Korea came from a publicly available website by the Korea Disease Control and Prevention Agency [50]. Finally, weekly time series of respiratory infection cases in the US were obtained from the Centers for

633 Disease Control and Prevention, National Respiratory and Enteric Virus Surveillance
634 System. Time series on number of tests were also available in Canada, Hong Kong,
635 and the US, but not in Korea.

636 Data processing

637 For all time series, we rounded every year to 52 weeks by taking the average number
638 of cases and tests between the 52nd and 53rd week. We also ~~reseale~~ ~~rescaled~~ all time
639 series to account for changes in testing patterns, which ~~are~~ ~~were~~ then used for the
640 actual analysis.

641 ~~Weekly time series of respiratory infection cases in Canada comes from the Respiratory~~
642 ~~Virus Detection Surveillance System, which collect data from select laboratories~~
643 ~~across Canada. We extract the data from . To account for For Canada, an increase in~~
644 ~~testing was observed from 2013 to 2024 , we calculate (Supplementary Figure S17).~~
645 ~~To account for this increase, we calculated a 2 year moving average for the number~~
646 ~~of tests for each pathogen, which we use used as a proxy for testing effort. Then,~~
647 ~~we divide divided the smoothed testing patterns by the smoothed value at the final~~
648 ~~week such that the testing effort has a maximum of 1. We then divide divided weekly~~
649 ~~cases by the testing effort to obtain a scaled case time series. A similar approach was~~
650 ~~used earlier for the an analysis of RSV time series in the US to account for changes~~
651 ~~in testing patterns [32].~~

652 ~~Weekly time series of respiratory infection cases in Hong Kong comes from the~~
653 ~~Centre for Health Protection, Department of Health. We extract the data from . We~~
654 ~~also apply the For Hong Kong, we applied the same scaling procedure to the time~~
655 ~~series as we did for Canada. For Hong Kong In this case, we only adjust adjusted~~
656 ~~for testing efforts up to the end of 2019 because there was a major reduction in testing for~~
657 ~~common respiratory pathogens since 2020. between 2020 and 2023 (Supplementary~~
658 ~~Figure S18).~~

659 ~~Weekly time series of acute respiratory infection cases in Korea comes from Korea~~
660 ~~Disease Control and Prevention Agency. We extract the data from . While we do~~
661 ~~For Korea, while we did not have information on testing, the reported number of~~
662 ~~respiratory infections consistently increased from 2013 to the end of 2019, which we~~
663 ~~interpreted as changes in testing patterns (Supplementary Figure S19). Since we~~
664 ~~do did not have testing numbers, we used the weekly sum of all acute respiratory~~
665 ~~viral infection cases as a proxy for testing, which were further smoothed with moving~~
666 ~~averaged average and scaled to have a maximum of 1. For Korea, we also only adjust~~
667 ~~adjusted for testing efforts up to the end of 2019.~~

668 ~~Finally, weekly time series of respiratory infection cases in the US comes from~~
669 ~~the National Respiratory and Enteric Virus Surveillance System. In the US, there~~
670 ~~has been a large increase in testing against for some respiratory pathogens, espe-~~
671 ~~cially RSV, which could not be corrected for through simple scaling by simple scaling~~
672 ~~(Supplementary Figure S20). Instead, we derive derived an incidence proxy by multi-~~
673 ~~plying the test positivity with influenza-like illness positivity, which is was taken from~~

674 <https://gis.cdc.gov/grasp/fluvview/fluportaldashboard.html>. This method
675 of estimating an incidence proxy has been recently applied in the analysis of seasonal
676 coronaviruses [15] and *Mycoplasma pneumoniae*-*Mycoplasma pneumoniae* infections
677 [12]. Detailed assumptions and justifications are provided in [51].

678 Data summary

679 To make qualitative comparisons between pre- and post-perturbation dynamics of
680 respiratory pathogen circulation patterns, we calculated the mean seasonal patterns
681 using time series of either rescaled cases or incidence proxy estimates before 2020. We
682 did so by taking the mean value in each week across all years before 2020. Confidence
683 intervals around the means were calculated using a simple t test.

684 Estimating pathogen resilience

685 In order to measure pathogen resilience from surveillance data, we first reconstruct
686 reconstructed the empirical pre-pandemic attractor of the system using Takens' em-
687 bedding theorem [23]. Specifically, for a given pathogen, we take-took the pre-
688 pandemic (before 2020) case time series $C(t)$ and reconstruct-reconstructed the at-
689 tractor using delayed embedding with a uniform delay of τ and dimension M :

$$X_{\tau,m}(t) = \langle \log(C(t) + 1), \log(C(t - \tau) + 1), \dots, \log(C(t - (M - 1)\tau) + 1) \rangle. \quad (2)$$

690 Here, the delay τ is determined by looking at was determined by calculating the
691 autocorrelation of the logged pre-pandemic time series and asking when the autocor-
692 relation crosses 0 for the first time [28]; a typical delay for for an annual outbreak is
693 around 13 weeks.

694 Then, for a given delay τ , we determine-determined the embedding dimension M
695 using the false nearest neighbors approach [27, 28]. To do so, we start-started with an
696 embedding dimension e and construct-constructed a set of points $A_{\tau,e} = \{X_{\tau,e}(t) | t <$
697 $2020\}$. Then, for each point $X_{\tau,e}(t)$, we determine-determined the nearest neighbor
698 from the set $A_{\tau,e}$, which we denote $X_{\tau,e}(t_{nn})$ for $t \neq t_{nn}$. Then, if the distance between
699 these two points on-in-the $e + 1$ dimension, $D_{\tau,e+1}(t) = \|X_{\tau,e+1}(t_{nn}) - X_{\tau,e+1}(t)\|_2$,
700 is larger than their distance on-in-the e dimension, $D_{\tau,e}(t) = \|X_{\tau,e}(t_{nn}) - X_{\tau,e}(t)\|_2$,
701 these two points are deemed to be false nearest neighbors; specifically, we use-used a
702 threshold R for the ratio between two distances $D_{\tau,e+1}(t)/D_{\tau,e}(t)$ to determine false
703 nearest neighbors. In the main text, we determine embedding dimension based as
704 the first dimension without The first embedding dimension e that does not have
705 any false nearest neighbors for $R = 10$. In Supplementary Materials, we impose
706 $R = 5$ to select for higher dimensions corresponds to the embedding dimension M
707 for a given pathogen-country pair. For the main analysis, we used $R = 10$, which
708 was chosen from a sensitivity analysis against simulated data (Supplementary Text).
709 Once we determine-determined the embedding lag τ and dimension M , we apply
710 the embedding to the entire time series and calculate the nearest neighbor distance

711 against the attractor $A_{\tau,M}$ to obtain a time series of distance from the attractor
 712 $D_{\tau,M}(t)$.

713 From a time series of distance from distances from the attractor, we estimate
 714 estimated pathogen resilience by fitting a linear regression to an appropriate window.
 715 To automatically select the fitting window, we begin fitting windows, we began by
 716 smoothing the distance time series using locally estimated scatterplot smoothing
 717 (LOESS) to obtain $\hat{D}_{\tau,M}(t)$, where the smoothing is performed on a log scale and
 718 exponentiated afterwards. This smoothing allowed us to find appropriate threshold
 719 values for selecting fitting windows that are insensitive to errors in our estimates of
 720 distance from the attractor. Then, we determine determined threshold values (T_{start}
 721 and T_{end}) for the smoothed distances and choose the fitting window based on when
 722 $\hat{D}_{\tau,M}(t)$ crosses these threshold values for the first time. These thresholds are were
 723 determined by first calculating the maximum distance,

$$\max \hat{D} = \max \hat{D}_{\tau,M}(t), \quad (3)$$

724 and the mean pre-pandemic distance,

$$\hat{D}_{\text{mean}} = \frac{1}{N_{t < 2020}} \sum_{t < 2020} \hat{D}_{\tau,M}(t), \quad (4)$$

725 as a reference, and then dividing their ratios into 10 equal bins: K equal bins,

$$T_{\text{start}} = \hat{D}_{\text{mean}} \times \left(\frac{\max \hat{D}}{\hat{D}_{\text{mean}}} \right)^{\frac{9/10(K-a)/K}{\text{~~~~~}}}, \quad (5)$$

$$T_{\text{end}} = \hat{D}_{\text{mean}} \times \left(\frac{\max \hat{D}}{\hat{D}_{\text{mean}}} \right)^{\frac{1/10a/K}{\text{~~~~~}}}, \quad (6)$$

726 where a represents the truncation threshold. This allows us to discard the initial
 727 period during which the distance increases (from the introduction of intervention
 728 measures) and the final period during which the distance plateaus (as the system
 729 reaches an attractor). The fitting window is determined based on when the smoothed
 730 distance $\hat{D}_{\tau,M}(t)$ crosses these threshold values for the first time; then, we fit a
 731 linear regression to logged (unsmoothed) distances $\log D_{\tau,M}(t)$ using that window.
 732 Alongside the threshold R for the false nearest neighbors approach, we tested optimal
 733 choices for K and a values using simulations (Supplementary Text). We used $K = 19$
 734 and $a = 2$ throughout the paper based on the simulation results.

735 Mathematical modeling

736 Throughout the paper, we use a series of mathematical models to illustrate the
 737 concept of pathogen resilience and to understand the determinants of pathogen re-
 738 silience. In general, the intrinsic resilience for of a given system is given by the largest

739 real part of the eigenvalues of the linearized system at endemic equilibrium. Here,
 740 we focus on the SIRS model ~~and with demography (birth and death) and~~ present
 741 the details of other models in Supplementary ~~MaterialsText~~. The SIRS (Susceptible-
 742 Infected-Recovered-Susceptible) model is the simplest model that allows for waning
 743 of immunity, where recovered (immune) individuals are assumed to become fully
 744 susceptible after an average of $1/\delta$ time period. The dynamics of the SIRS model is
 745 described by the following set of differential equations:

$$\frac{dS}{dt} = \mu - \beta(t)SI - \mu S + \delta R \quad (7)$$

$$\frac{dI}{dt} = \beta(t)SI - (\gamma + \mu)I \quad (8)$$

$$\frac{dR}{dt} = \gamma I - (\delta + \mu)R \quad (9)$$

746 where μ represents the birth ~~death rate and death rates~~, $\beta(t)$ represents the time-
 747 varying transmission rate, and γ represents the recovery rate. The basic reproduction
 748 number ~~$R_0 = \beta(t)/(\gamma + \mu)$~~ $R_0(t) = \beta(t)/(\gamma + \mu)$ is defined as the average number of
 749 secondary infections ~~caused by that~~ a single infected individual ~~would cause~~ in a
 750 fully susceptible population ~~at time t~~ and measures the intrinsic transmissibility of
 751 a pathogen.

752 When we ~~first introduce introduced~~ introduced the idea of pathogen resilience (Figure 2), we
 753 ~~impose imposed~~ sinusoidal changes to the transmission rate to account for seasonal
 754 transmission~~–~~,

$$\beta(t) = b_1(1 + \theta \cos(2\pi(t - \phi)))\alpha(t), \quad (10)$$

755 where b_1 represents the baseline transmission rate, θ represents the seasonal amplitude,
 756 and ϕ represents the seasonal offset term. Here, we also ~~introduce introduced~~ an
 757 extra multiplicative term $\alpha(t)$ to account for the impact of ~~COVID-19 interventions pandemic~~
 758 ~~perturbations~~, where $\alpha(t) < 1$ indicates transmission reduction. Figure 2A and 2B
 759 ~~are were~~ generated assuming $b_1 = 3 \times (365/7 + 1/50)/\text{years}$, $\theta = 0.2$, $\phi = 0$, $\mu =$
 760 $1/50/\text{years}$, $\gamma = 365/7/\text{years}$, and $\delta = 1/2/\text{years}$. Specifically, $b_1 = 3 \times (365/7 + 1/50)/\text{years}$
 761 implies $R_0 = 3$, where ~~(365/7 + 1/50)/years represent the rate of recovery~~. In Figure
 762 2A, we ~~impose imposed~~ a 50% transmission reduction for 6 months from 2020:

$$\alpha(t) = \begin{cases} 0.5 & 2020 \leq t < 2020.5 \\ 1 & \text{otherwise} \end{cases} \quad (11)$$

763 In Figure 2B, we ~~impose imposed~~ a 50% transmission reduction for 6 months from
 764 2020 and a permanent 10% reduction onward:

$$\alpha(t) = \begin{cases} 1 & t < 2020 \\ 0.5 & 2020 \leq t < 2020.5 \\ 0.9 & 2020.5 \leq t \end{cases} \quad (12)$$

765 In both scenarios, we ~~simulate~~ simulated the SIRS model from the ~~following same~~
 766 initial conditions ($S(0) = 1/\mathcal{R}_0$, $I(0) = 1 \times 10^{-6}$, and $R(0) = 1 - S(0) - I(0)$) from
 767 1900 until 2030. ~~Throughout the paper, all deterministic models were solved using~~
 768 ~~the lsoda solver from the deSolve package [52] in R [53]~~.

769 To measure the empirical resilience of the ~~SIR~~-SIRS model (Figure 2C and
 770 2F), we ~~compute~~ computed the normalized distance between post-intervention sus-
 771 ceptible and logged infected proportions and their corresponding ~~pre-intervention~~
 772 ~~unperturbed~~ values at the same time ~~of year~~:

$$\sqrt{\left(\frac{S(t) - S_{\text{pre}}(t)}{\sigma_S}\right)^2 + \left(\frac{\log I(t) - \log I_{\text{pre}}(t)}{\sigma_{\log I}}\right)^2} \sqrt{\left(\frac{S(t) - S_{\text{unperturbed}}(t)}{\sigma_S}\right)^2 + \left(\frac{\log I(t) - \log I_{\text{unperturbed}}(t)}{\sigma_{\log I}}\right)^2} \quad (13)$$

773 where σ_S and $\sigma_{\log I}$ represent the standard deviation in the ~~pre-intervention~~-~~unperturbed~~
 774 susceptible and logged infected proportions. ~~We normalize~~ The unperturbed values
 775 were obtained by simulating the same SIRS model without pandemic perturbations
 776 ($\alpha = 1$). We normalized the differences in susceptible and logged infected propor-
 777 tions to allow both quantities to equally contribute to the changes in distance from
 778 ~~attractor~~-~~the attractor~~. We used logged prevalence, instead of absolute prevalence,
 779 in order to capture epidemic dynamics in deep troughs during the intervention period.
 780 In Supplementary Materials, we also ~~compare~~ the compared how the degree of sea-
 781 sonal transmission affects empirical resilience by varying θ from 0 to 0.4; when we
 782 ~~assume~~ assumed no seasonality ($\theta = 0$), we ~~do~~ did not normalize the distance because
 783 the standard deviation of pre-intervention dynamics are zero.

784 Finally, we use ~~We used~~ the SIRS model to understand how underlying epidemi-
 785 logical parameters affect pathogen resilience and ~~link this~~ determine the relationship
 786 to underlying susceptible host dynamics. For the simple SIRS model without sea-
 787 sonal transmission ($\theta = 0$), the intrinsic resilience ~~corresponds to~~ equals

$$-\frac{\text{Re}(\lambda)}{2} = \frac{\delta + \beta I^* + \mu}{2}. \quad (14)$$

788 Here, I^* represents the prevalence ~~values~~ at endemic equilibrium:

$$I^* = \frac{(\delta + \mu)(\beta - (\gamma + \mu))}{\beta(\delta + \gamma + \mu)}. \quad (15)$$

789 The susceptible replenishment rate is given by ~~+~~

$$S_{\text{replenish}} = \frac{\mu + \delta R}{S^*}, \quad (16)$$

790 where $S^* = 1/\mathcal{R}_0$ represents the equilibrium proportion of susceptible individuals.
 791 We ~~vary~~ varied the basic reproduction number \mathcal{R}_0 between 1.1 to 6 and the average
 792 duration of immunity $1/\delta$ between 2 to ~~80-4~~ years, and ~~compute~~ computed these
 793 two quantities. In doing so, we ~~fix~~ fixed all other parameters: $\mu = 1/80/\text{years}$ and

794 $\gamma = 365/7/\text{years}$. When infection provides a life-long immunity ($\delta = 0$), the intrinsic
795 resilience is inversely proportional to the susceptible replenishment rate:

$$-\frac{\text{Re}(\lambda)}{2} = \frac{\mu}{2S^*} = \frac{S_{\text{replenish}}}{2}. \quad (17)$$

796 Finally, we used a seasonally unforced stochastic SIRS model without demography
797 to understand how pathogen resilience affects sensitivity of the system to demographic
798 stochasticity (see Supplementary Text for the details of the stochastic SIRS model).
799 By varying the basic reproduction number \mathcal{R}_0 between 2 to 20 and the average
800 duration of immunity $1/\delta$ between 1 to 40 years, we ran the SIRS model for 100 years
801 and computed the epidemic amplitude, which we defined as $(\max I - \min I)/(2I)$.
802 Each simulation began from the equilibrium, and we truncated the initial 25 years
803 before computing the epidemic amplitude. In doing so, we assumed $\gamma = 365/7/\text{years}$
804 and fixed the population size to 1 billion to prevent any fadeouts. We also considered
805 a seasonally forced stochastic SIRS model without demography, assuming an amplitude
806 of seasonal forcing of 0.04; in this case, we computed the relative epidemic amplitude
807 by comparing the deterministic and stochastic trajectories (Supplementary Materials).

808

809 Acknowledgement

810 We thank Anthony R. Ives and Stefano Allesina for helpful discussion. We thank
811 Centers for Disease Control and Prevention, National Respiratory and Enteric Virus
812 Surveillance System for providing respiratory case data in the US.

813 Data availability

814 All data and code are stored in a publicly available GitHub repository (<https://github.com/cobeylab/return-time>).

816 Funding

817 S.W.P. is a Peter and Carmen Lucia Buck Foundation Awardee of the Life Sciences
818 Research Foundation. B.F.N. acknowledges financial support from the Carlsberg
819 Foundation (grant no. CF23-0173). B.T.G. is supported by Princeton Catalysis
820 Initiative and Princeton Precision Health. S.C. is supported by Federal funds from
821 the National Institute of Allergy and Infectious Diseases, National Institutes of
822 Health, Department of Health and Human Services under CEIRR contract 75N93021C00015.
823 The content is solely the responsibility of the authors and does not necessarily
824 represent the official views of the NIAID or the National Institutes of Health. This
825 project has been funded in whole or in part with Federal funds from the National

826 Cancer Institute, National Institutes of Health, under Prime Contract No. 75N91019D00024,
827 Task Order No. 75N91023F00016 (B.F.N., E.H., and B.T.G). The content of this
828 publication does not necessarily reflect the views or policies of the Department of
829 Health and Human Services, nor does mention of trade names, commercial products
830 or organizations imply endorsement by the U.S. Government.

831 **Supplementary Text**

832 **Resilience of a stage-structured system.**

833 In Figure 2G–I, we ~~use~~used a more realistic, stage-structured model to illustrate how
 834 transient phenomena can cause the system to slow down. Specifically, we ~~use~~used
 835 the stage-structured RSV model proposed by [32], which assumes that subsequent
 836 reinfections cause an individual to become less susceptible and transmissible than
 837 previous infections. In contrast to a standard SIRS model, this model does not
 838 include a recovered compartment, which allow for temporary protection against new
 839 infections, and assumes that recoverd individuals are immediately susceptible to new
 840 infections. The model dynamics can be described as follows:

$$\frac{dM}{dt} = \mu - (\omega + \mu)M \quad (S1)$$

$$\frac{dS_0}{dt} = \omega M - (\lambda(t) + \mu)S_0 \quad (S2)$$

$$\frac{dI_1}{dt} = \lambda(t)S_0 - (\gamma_1 + \mu)I_1 \quad (S3)$$

$$\frac{dS_1}{dt} = \gamma_1 I_1 - (\sigma_1 \lambda(t) + \mu)S_1 \quad (S4)$$

$$\frac{dI_2}{dt} = \sigma_1 \lambda(t)S_1 - (\gamma_2 + \mu)I_2 \quad (S5)$$

$$\frac{dS_2}{dt} = \gamma_2 I_2 - (\sigma_2 \lambda(t) + \mu)S_2 \quad (S6)$$

$$\frac{dI_3}{dt} = \sigma_2 \lambda(t)S_2 - (\gamma_3 + \mu)I_3 \quad (S7)$$

$$\frac{dS_3}{dt} = \gamma_3 I_3 - (\sigma_3 \lambda(t) + \mu)S_3 + \gamma_4 I_4 \quad (S8)$$

$$\frac{dI_4}{dt} = \sigma_3 \lambda(t)S_3 - (\gamma_4 + \mu)I_4 \quad (S9)$$

841 where M represents the proportion of individuals who are maternally immune; S_i
 842 represents the proportion of individuals who are susceptible after i prior infections; I_i
 843 represents the proportion of individuals who are currently (re)-infected with their i -th
 844 infection; μ represents the birth and death rates; $1/\omega$ represents the mean duration
 845 of maternal immunity; $1/\gamma_i$ represents the mean duration of infection; $\lambda(t)$ represents
 846 the force of infection; and σ_i represents the reduction in susceptibility for the i -th
 847 reinfection. The force of infection is modeled using a sinusoidal function:

$$\beta(t) = b_1(1 + \theta \cos(2\pi(t - \phi)))\alpha(t) \quad (S10)$$

$$\lambda(t) = \beta(I_1 + \rho_1 I_2 + \rho_2(I_3 + I_4)), \quad (S11)$$

848 where b_1 represents the baseline transmission rate; θ represents the seasonal amplitude;
 849 ϕ represents the seasonal offset term; $\alpha(t)$ represents the intervention effect;

and ρ_i represents the impact of immunity on transmission reduction. We ~~use~~used the following parameters to simulate the impact of interventions on epidemic dynamics [32]: $b_1 = 9 \times (365/10 + 1/80)/\text{years}$, $\theta = 0.2$, $\phi = -0.1$, $\omega = 365/112/\text{years}$, $\gamma_1 = 365/10/\text{years}$, $\gamma_2 = 365/7/\text{years}$, $\gamma_3 = 365/5/\text{years}$, $\sigma_1 = 0.76$, $\sigma_2 = 0.6$, $\sigma_3 = 0.4$, $\rho_1 = 0.75$, $\rho_2 = 0.51$, and $\mu = 1/80/\text{years}$. We ~~assume~~assumed a 50% transmission reduction for 6 months from 2020:

$$\alpha(t) = \begin{cases} 0.5 & 2020 \leq t < 2020.5 \\ 1 & \text{otherwise} \end{cases} \quad (\text{S12})$$

The model ~~is~~was simulated from 1900 to 2030 using the following initial conditions: $M = 0$, $S_0 = 1/\mathcal{R}_0 - I_1$, $I_1 = 1 \times 10^{-6}$, ~~$S_1 = 1 - 1/\mathcal{R}_0$~~ , $S_1 = 1 - 1/\mathcal{R}_0$, $I_2 = 0$, $S_2 = 0$, $I_3 = 0$, $S_3 = 0$, and $I_4 = 0$. For the phase plane analysis (Figure 2H) and distance analysis (Figure 2I), we ~~rely~~relied on the average susceptibility,

$$\bar{S} = S_0 + \sigma_1 S_1 + \sigma_2 S_2 + \sigma_3 S_3, \quad (\text{S13})$$

and total prevalence,

$$I_{\text{total}} = I_1 + I_2 + I_3 + I_4. \quad (\text{S14})$$

These quantities ~~are~~were used to compute the normalized distance from the attractor, as described in the main text.

Resilience of a multistrain system.

We ~~use~~used a simple two-strain model to show that a multistrain host-pathogen system that is coupled through cross immunity can be described by a single resilience value. The model dynamics can be described as follows [34]:

$$\frac{dS}{dt} = \mu - \mu S - (\lambda_1 + \lambda_2)S + \underline{\rho} \underline{\delta}_1 R_1 + \underline{\rho} \underline{\delta}_2 R_2 \quad (\text{S15})$$

$$\frac{dI_1}{dt} = \lambda_1 S - (\gamma_1 + \underline{m} \underline{u} \underline{\mu}) I_1 \quad (\text{S16})$$

$$\frac{dI_2}{dt} = \lambda_2 S - (\gamma_2 + \underline{m} \underline{u} \underline{\mu}) I_2 \quad (\text{S17})$$

$$\frac{dR_1}{dt} = \gamma_1 I_1 - \lambda_2 \epsilon_{21} R_1 - \underline{\rho} \underline{\delta}_1 R_1 + \underline{\rho} \underline{\delta}_2 R - \mu R_1 \quad (\text{S18})$$

$$\frac{dR_2}{dt} = \gamma_2 I_2 - \lambda_1 \epsilon_{12} R_2 - \underline{\rho} \underline{\delta}_2 R_2 + \underline{\rho} \underline{\delta}_1 R - \mu R_2 \quad (\text{S19})$$

$$\frac{dJ_1}{dt} = \lambda_1 \epsilon_{12} R_2 - (\gamma_1 + \mu) J_1 \quad (\text{S20})$$

$$\frac{dJ_2}{dt} = \lambda_2 \epsilon_{21} R_1 - (\gamma_2 + \mu) J_2 \quad (\text{S21})$$

$$\frac{dR}{dt} = \gamma_1 J_1 + \gamma_2 J_2 - \underline{\rho} \underline{\delta}_1 R - \underline{\rho} \underline{\delta}_2 R - \mu R \quad (\text{S22})$$

where S represents the proportion of individuals who are fully susceptible to infections by both strains; I_1 represents the proportion of individuals who are infected with strain 1 without prior immunity; I_2 represents the proportion of individuals who are infected with strain 2 without prior immunity; R_1 represents the proportion of individuals who are fully immune against strain 1 and partially susceptible to reinfection by strain 2; R_2 represents the proportion of individuals who are fully immune against strain 2 and partially susceptible to reinfection by strain 1; J_1 represents the proportion of individuals who are infected with strain 1 with prior immunity against strain 2; J_2 represents the proportion of individuals who are infected with strain 2 with prior immunity against strain 1; R represents the proportion of individuals who are immune to infections from both strains; μ represents the birth/death rate; λ_1 and λ_2 represent the force of infection from strains 1 and 2, respectively; ρ_1 and ρ_2 represent the waning immunity rate; γ_1 and γ_2 represent the recovery rate; ϵ_{21} and ϵ_{12} represent the susceptibility to reinfection with strains 2 and 1, respectively, given prior immunity from infection with strains 1 and 2, respectively. The force of infection is modeled as follows:

$$\beta_1 = b_1(1 + \theta_1 \sin(2\pi(t - \phi_1)))\alpha(t) \quad (\text{S23})$$

$$\beta_2 = b_2(1 + \theta_2 \sin(2\pi(t - \phi_2)))\alpha(t) \quad (\text{S24})$$

$$\lambda_1 = \beta_1(I_1 + J_1) \quad (\text{S25})$$

$$\lambda_2 = \beta_2(I_2 + J_2) \quad (\text{S26})$$

In Supplementary Figures S2–S4, we assume assumed the following parameters: $b_1 = 2 \times 52/\text{years}$, $b_2 = 4 \times 52/\text{years}$, $\phi_1 = \phi_2 = 0$, $\epsilon_{12} = 0.9$, $\epsilon_{21} = 0.5$, $\gamma_1 = \gamma_2 = 52/\text{years}$, $\rho_1 = \rho_2 = 1/\text{years}$, $\delta_1 = \delta_2 = 1/\text{years}$, and $\mu = 1/70/\text{years}$. For all simulations, we assume assumed a 50% transmission reduction for 6 months from 2020:

$$\alpha(t) = \begin{cases} 0.5 & 2020 \leq t < 2020.5 \\ 1 & \text{otherwise} \end{cases} \quad (\text{S27})$$

The seasonal amplitude θ is varied from 0 to 0.4. All simulations are ran were run from 1900 to 2030 from the with following initial conditions: $S(0) = 1 - 2 \times 10^{-6}$, $I_1(0) = 1 \times 10^{-6}$, $I_2(0) = 1 \times 10^{-6}$, $R_1(0) = 0$, $R_2(0) = 0$, $J_1(0) = 0$, $J_2(0) = 0$, and $R(0) = 0$.

For this, we consider three different We considered three scenarios for measuring pathogen resilience: (1) we only have information about strain 1, (2) we only have information about strain 2, and (3) we are unable to distinguish the differences between strains. In the first two scenarios (see panels A–C for strain 1 and panels D–F for strain 2), we eonsider considered the dynamics of average susceptibility for each strain and total prevalence:

$$\bar{S}_1 = S + \epsilon_{12}R_2 \quad (\text{S28})$$

$$\hat{I}_1 = I_1 + J_1 \quad (\text{S29})$$

$$\bar{S}_2 = S + \epsilon_{21} R_1 \quad (\text{S30})$$

$$\hat{I}_2 = I_2 + J_2 \quad (\text{S31})$$

897 In the third scenario (panels G–I), we ~~considered~~ considered the dynamics of total
 898 susceptible and infected ~~population~~ populations:

$$\hat{S} = S + R_2 + R_1 \quad (\text{S32})$$

$$\hat{I} = I_1 + J_1 + I_2 + J_2 \quad (\text{S33})$$

899 These quantities ~~were~~ used to compute the normalized distance from the attractor,
 900 as described in the main text.

901 Estimating intrinsic resilience using a mechanistic model

902 We ~~test~~ tested whether we can reliably estimate the intrinsic resilience of a system
 903 by fitting a mechanistic model. Specifically, we ~~simulate~~ simulated case time series
 904 from stochastic SIRS and two-strain models and ~~fit~~ fitted a simple, deterministic
 905 SIRS model using a Bayesian framework [12, 29, 54].

906 First, we describe the simulation set up. The stochastic SIRS model can be
 907 written as follows. We simulated the models in discrete time with a daily time step
 908 ($\Delta t = 1$), incorporating demographic stochasticity:

$$\beta(t) = \mathcal{R}_0 \left(1 + \theta \cos \left(\frac{2\pi t}{364} \right) \right) \alpha(t)(1 - \exp(-\gamma)) \quad (\text{S34})$$

$$\text{FOI}(t) = \beta(t)I(t - \Delta t)/N \quad (\text{S35})$$

$$B(t) \sim \text{Poisson}(\mu N) \quad (\text{S36})$$

$$\Delta S(t) \sim \text{Binom}(S(t - \Delta t), 1 - \exp(-(\text{FOI}(t) + \mu)\Delta t)) \quad (\text{S37})$$

$$N_{SI}(t) \sim \text{Binom}\left(\Delta S(t), \frac{\text{FOI}(t)}{\text{FOI}(t) + \mu}\right) \quad (\text{S38})$$

$$\Delta I(t) \sim \text{Binom}(I(t - \Delta t), 1 - \exp(-(\gamma + \mu)\Delta t)) \quad (\text{S39})$$

$$N_{IR}(t) \sim \text{Binom}\left(\Delta I(t), \frac{\gamma}{\gamma + \mu}\right) \quad (\text{S40})$$

$$\Delta R(t) \sim \text{Binom}(R(t - \Delta t), 1 - \exp(-(\delta + \mu)\Delta t)) \quad (\text{S41})$$

$$N_{RS}(t) \sim \text{Binom}\left(\Delta R(t), \frac{\delta}{\delta + \mu}\right) \quad (\text{S42})$$

$$S(t) = S(t - \Delta t) + N_{RS}(t) + B(t) - \Delta S(t) \quad (\text{S43})$$

$$I(t) = I(t - \Delta t) + N_{SI}(t) - \Delta I(t) \quad (\text{S44})$$

$$R(t) = R(t - \Delta t) + N_{IR}(t) - \Delta R(t) \quad (\text{S45})$$

909 where FOI ~~represents~~ represents the force of infection; N_{ij} ~~represents~~ represents the
 910 number of individuals moving from compartment i to j on a given day; and $B(t)$

911 represents the number of new births. We simulate All other parameters definitions
 912 can be found in the description of the deterministic version of the model. We
 913 simulated the model on a daily scale—assuming 364 days in a year so that it can
 914 be evenly grouped into 52 weeks—with the following parameters: $\mathcal{R}_0 = 3$, $\theta = 0.1$,
 915 $\gamma = 1/7/\text{days}$, $\delta = 1/(364 \times 2)/\text{days}$, $\mu = 1/(364 \times 50)/\text{days}$, and $N = 1 \times 10^8$.
 916 The model is-was simulated from 1900 to 2030 assuming $S(0) = N/3$, $I(0) = 100$,
 917 and $R(0) = N - S(0) - I(0)$. The observed incidence from the model is-was then
 918 simulated as follows:

$$C(t) = \text{Beta-BinomBeta-Binom}(N_{SI}(t), \rho, k), \quad (\text{S46})$$

919 where ρ represents the reporting probability and k represents the overdispersion
 920 parameter of beta-binomial distribution. We assume Here, we used the beta-binomial
 921 distribution to account for overdispersion in reporting. We assumed $\rho = 0.002$ (i.e.,
 922 0.2% probability) and $k = 1000$.

923 The stochastic We used an analogous approach for the two-strain modelcan be
 924 written as follows:

$$\beta_1(t) = b_1 \left(1 + \theta_1 \cos \left(\frac{2\pi(t - \phi_1)}{364} \right) \right) \alpha(t) \quad (\text{S47})$$

$$\beta_2(t) = b_2 \left(1 + \theta_2 \cos \left(\frac{2\pi(t - \phi_2)}{364} \right) \right) \alpha(t) \quad (\text{S48})$$

$$\text{FOI}_1(t) = \beta_1(t)(I_1(t - \Delta t) + J_1(t - \Delta t))/N \quad (\text{S49})$$

$$\text{FOI}_2(t) = \beta_2(t)(I_2(t - \Delta t) + J_2(t - \Delta t))/N \quad (\text{S50})$$

$$B(t) \sim \text{Poisson}(\mu N) \quad (\text{S51})$$

$$\Delta S(t) \sim \text{Binom}(S(t - \Delta t), 1 - \exp(-(\text{FOI}_1(t) + \text{FOI}_2(t) + \mu)\Delta t)) \quad (\text{S52})$$

$$N_{SI_1}(t) \sim \text{Binom}\left(\Delta S(t), \frac{\text{FOI}_1(t)}{\text{FOI}_1(t) + \text{FOI}_2(t) + \mu}\right) \quad (\text{S53})$$

$$N_{SI_2}(t) \sim \text{Binom}\left(\Delta S(t), \frac{\text{FOI}_2(t)}{\text{FOI}_1(t) + \text{FOI}_2(t) + \mu}\right) \quad (\text{S54})$$

$$\Delta I_1(t) \sim \text{Binom}(I_1(t - \Delta t), 1 - \exp(-(\gamma_1 + \mu)\Delta t)) \quad (\text{S55})$$

$$N_{I_1 R_1}(t) \sim \text{Binom}\left(\Delta I_1(t), \frac{\gamma_1}{\gamma_1 + \mu}\right) \quad (\text{S56})$$

$$\Delta I_2(t) \sim \text{Binom}(I_2(t - \Delta t), 1 - \exp(-(\gamma_2 + \mu)\Delta t)) \quad (\text{S57})$$

$$N_{I_2 R_2}(t) \sim \text{Binom}\left(\Delta I_2(t), \frac{\gamma_2}{\gamma_2 + \mu}\right) \quad (\text{S58})$$

$$\Delta R_1(t) \sim \text{Binom}(R_1(t - \Delta t), 1 - \exp(-(\epsilon_{21}\text{FOI}_2(t) + \rho_1 + \mu)\Delta t)) \quad (\text{S59})$$

$$N_{R_1 S}(t) \sim \text{Binom}\left(\Delta R_1(t), \frac{\rho_1}{\epsilon_{21}\text{FOI}_2(t) + \rho_1 + \mu}\right) \quad (\text{S60})$$

$$N_{R_1 J_2}(t) \sim \text{Binom}\left(\Delta R_1(t), \frac{\epsilon_{21}\text{FOI}_2(t)}{\epsilon_{21}\text{FOI}_2(t) + \rho_1 + \mu}\right) \quad (\text{S61})$$

$$\Delta R_2(t) \sim \text{Binom}(R_2(t - \Delta t), 1 - \exp(-(\epsilon_{12}\text{FOI}_1(t) + \rho_2 + \mu)\Delta t)) \quad (\text{S62})$$

$$N_{R_2S}(t) \sim \text{Binom}\left(\Delta R_2(t), \frac{\rho_2}{\epsilon_{12}\text{FOI}_1(t) + \rho_2 + \mu}\right) \quad (\text{S63})$$

$$N_{R_2J_1}(t) \sim \text{Binom}\left(\Delta R_2(t), \frac{\epsilon_{12}\text{FOI}_1(t)}{\epsilon_{12}\text{FOI}_1(t) + \rho_2 + \mu}\right) \quad (\text{S64})$$

$$\Delta J_1(t) \sim \text{Binom}(J_1(t - \Delta t), 1 - \exp(-(\gamma_1 + \mu)\Delta t)) \quad (\text{S65})$$

$$N_{J_1R}(t) \sim \text{Binom}\left(\Delta J_1(t), \frac{\gamma_1}{\gamma_1 + \mu}\right) \quad (\text{S66})$$

$$\Delta J_2(t) \sim \text{Binom}(J_2(t - \Delta t), 1 - \exp(-(\gamma_2 + \mu)\Delta t)) \quad (\text{S67})$$

$$N_{J_2R}(t) \sim \text{Binom}\left(\Delta J_2(t), \frac{\gamma_2}{\gamma_2 + \mu}\right) \quad (\text{S68})$$

$$\Delta R(t) \sim \text{Binom}(R(t - \Delta t), 1 - \exp(-(\rho_1 + \rho_2 + \mu)\Delta t)) \quad (\text{S69})$$

$$N_{RR_1}(t) \sim \text{Binom}\left(\Delta R(t), \frac{\rho_1}{\rho_1 + \rho_2 + \mu}\right) \quad (\text{S70})$$

$$N_{RR_2}(t) \sim \text{Binom}\left(\Delta R(t), \frac{\rho_2}{\rho_1 + \rho_2 + \mu}\right) \quad (\text{S71})$$

$$S(t) = S(t - \Delta t) - \Delta S(t) + B(t) + N_{R_1S}(t) + N_{R_2S}(t) \quad (\text{S72})$$

$$I_1(t) = I_1(t - \Delta t) - \Delta I_1(t) + N_{SI_1}(t) \quad (\text{S73})$$

$$I_2(t) = I_2(t - \Delta t) - \Delta I_2(t) + N_{SI_2}(t) \quad (\text{S74})$$

$$R_1(t) = R_1(t - \Delta t) - \Delta R_1(t) + N_{I_1R_1}(t) + N_{RR_1}(t) \quad (\text{S75})$$

$$R_2(t) = R_2(t - \Delta t) - \Delta R_2(t) + N_{I_2R_2}(t) + N_{RR_2}(t) \quad (\text{S76})$$

$$J_1(t) = J_1(t - \Delta t) - \Delta J_1(t) + N_{R_2J_1}(t) \quad (\text{S77})$$

$$J_2(t) = J_2(t - \Delta t) - \Delta J_2(t) + N_{R_1J_2}(t) \quad (\text{S78})$$

$$R(t) = R(t - \Delta t) - \Delta R(t) + N_{J_1R}(t) + N_{J_2R}(t) \quad (\text{S79})$$

We simulated the model on a daily scale with previously estimated parameters for the RSV-HMPV interaction [34]: $b_1 = 1.7/\text{weeks}$, $b_2 = 1.95/\text{weeks}$, $\theta_1 = 0.4$, $\theta_2 = 0.3$, $\phi_1 = 0.005 \times 7/364$, $\phi_2 = 4.99 \times 7/364$, $\epsilon_{12} = 0.92$, $\epsilon_{21} = 0.45$, $\gamma_1 = 1/10/\text{days}$, $\gamma_2 = 1/10/\text{days}$, $\rho_1 = 1/364/\text{days}$, $\rho_2 = 1/364/\text{days}$, $\mu = 1/(70 \times 364)/\text{days}$, and $N = 1 \times 10^8$. The model is simulated from 1900 to 2030 assuming $S(0) = N - 200$, $I_1(0) = 100$, $I_2(0) = 100$, $R_1(0) = 0$, $R_2(0) = 0$, $J_1(0) = 0$, $J_2(0) = 0$, and $R(0) = 0$. The observed incidence for each strain is then simulated as follows:

$$C_1(t) = \text{Beta - BinomBeta-Binom}(N_{SI_1}(t) + N_{R_2J_1}, \rho, k), \quad (\text{S80})$$

$$C_2(t) = \text{Beta - BinomBeta-Binom}(N_{SI_2}(t) + N_{R_1J_2}, \rho, k), \quad (\text{S81})$$

where ρ represents the reporting probability and k represents the overdispersion parameter of beta-binomial distribution. We assume $\rho = 0.002$ (i.e., 0.2%

935 probability) and $k = 500$. We also ~~considered~~ considered the total incidence: $C_{\text{total}}(t) =$
 936 $C_1(t) + C_2(t)$.

937 For both models, we ~~considered~~ ~~a more realistic challenges in intervention effects~~
 938 ~~considered a more realistically shaped pandemic perturbation~~ $\alpha(t)$ to challenge our
 939 ability to estimate the intervention effects. Thus, we ~~assumed~~ assumed a 40% trans-
 940 mission reduction for 3 months from March 2020, followed by a 10% transmission
 941 reduction for 6 months, 20% transmission reduction for 3 months, and a final return
 942 to normal levels:

$$\alpha(t) = \begin{cases} 1 & t < 2020.25 \\ 0.6 & 2020.25 \leq t < 2020.5 \\ 0.9 & 2020.5 \leq t < 2021 \\ 0.8 & 2021 \leq t < 2021.25 \\ 1 & 2021.25 \leq t \end{cases}. \quad (\text{S82})$$

943 For all simulations, we ~~truncate~~ truncated the time series from the beginning of 2014
 944 to the end of 2023 and ~~aggregate~~ aggregated them into weekly cases.

945 To infer intrinsic resilience from time series, we ~~fit~~ fitted a simple discrete time,
 946 deterministic SIRS model ~~in a Bayesian framework~~ [12]:

$$\Delta t = 1 \text{ week} \quad (\text{S83})$$

$$\text{FOI}(t) = \beta(t)(I(t - \Delta t) + \omega)/N \quad (\text{S84})$$

$$\Delta S(t) = [1 - \exp(-(\text{FOI}(t) + \mu)\Delta t)] S(t - \Delta t) \quad (\text{S85})$$

$$N_{SI}(t) = \frac{\text{FOI}(t)\Delta S(t)}{\text{FOI}(t) + \mu} \quad (\text{S86})$$

$$\Delta I(t) = [1 - \exp(-(\gamma + \mu)\Delta t)] I(t - \Delta t) \quad (\text{S87})$$

$$N_{IR}(t) = \frac{\gamma \Delta I(t)}{\gamma + \mu} \quad (\text{S88})$$

$$\Delta R(t) = [1 - \exp(-(\nu + \mu)\Delta t)] R(t - \Delta t) \quad (\text{S89})$$

$$N_{RS}(t) = \frac{\nu \Delta R(t)}{\nu + \mu} \quad (\text{S90})$$

$$S(t) = S(t - \Delta t) + \mu S - \Delta S(t) + N_{RS}(t) \quad (\text{S91})$$

$$I(t) = I(t - \Delta t) - \Delta I(t) + N_{SI}(t) \quad (\text{S92})$$

$$R(t) = R(t - \Delta t) - \Delta R(t) + N_{IR}(t) \quad (\text{S93})$$

947 where we include an extra term ω to account for ~~external infections~~ importation. Al-
 948 though actual simulations ~~do~~ did not include any ~~external infections~~, we importation,
 949 we had found that including this term generally helped with model convergence in
 950 previous analyses [12]. The transmission rate ~~is~~ was divided into a seasonal term
 951 $\beta_{\text{seas}}(t)$ (repeated every year) and intervention term $\alpha(t)$, which ~~are~~ were estimated
 952 jointly:

$$\beta(t) = \beta_{\text{seas}}(t)\alpha(t), \quad (\text{S94})$$

953 where $\alpha < 1$ corresponds to reduction in transmission due to intervention effects. To
 954 constrain the smoothness of $\beta_{\text{seas}}(t)$, we impose imposed cyclic, random-walk priors:

$$\beta_{\text{seas}}(t) \sim \text{Normal}(\beta_{\text{seas}}(t-1), \sigma) \quad t = 2 \dots 52 \quad (\text{S95})$$

$$\beta_{\text{seas}}(1) \sim \text{Normal}(\beta_{\text{seas}}(52), \sigma) \quad (\text{S96})$$

$$\underline{\sigma} \sim \text{Half-Normal}(0, 1) \quad (\text{S97})$$

955 We fix We fixed $\alpha(t) = 1$ for all $t < 2020$ and estimate α assuming a normal prior:

$$\alpha \sim \text{Normal}(1, 0.25). \quad (\text{S98})$$

956 We assume assumed weakly informative priors on ω and τ :

$$\omega \sim \text{Normal}(0, 200) \quad \tau \sim \text{Half-Normal}(0, 200) \quad (\text{S99})$$

$$\nu \sim \text{Normal}(104, 26) \quad (\text{S100})$$

957 We assume assumed that the true birth/death rates, population sizes, and recovery
 958 rates are known. We note, however, that assuming $\gamma = 1/\text{week}$ actually correspond
 959 corresponds to a mean simulated infectious period of 1.6 weeks due to a time discretization,
 960 which is much longer than the true value; this approximation allows us to test whether
 961 we can still robustly estimate the intrinsic resilience given parameters parameter mis-
 962 specification. Initial conditions are were estimated with following priors:

$$S(0) = Ns(0) \quad (\text{S101})$$

$$I(0) = Ni(0) \quad (\text{S102})$$

$$s(0) \sim \text{Uniform}(0, 1) \quad (\text{S103})$$

$$i(0) \sim \text{Half-Normal}(0, 0.001) \quad (\text{S104})$$

963 Finally, the Observation model is observation model was specified as follows:

$$\text{Cases}(t) \sim \text{Negative-Binomial}(\rho N_{SI}(t), \phi) \quad (\text{S105})$$

$$\rho \sim \text{Half-Normal}(0, 0.02) \quad (\text{S106})$$

$$\phi \sim \text{Half-Normal}(0, 10) \quad (\text{S107})$$

964 where ρ represents the reporting probability and ϕ represents the negative binomial
 965 overdispersion parameter.

966 The model is was fitted to four separate time series: (1) incidence time series from
 967 the SIRS model, (2) incidence time series for strain 1 from the two-strain model,
 968 (3) incidence time series for strain 2 from the two-strain model, and (4) combined
 969 incidence time series for strains 1 and 2 from the two-strain model. The model was
 970 fitted using rstan [55, 56] with 4 chains, each consisting of 2000 iterations. The
 971 resulting posterior distribution was used to calculate the intrinsic resilience of the
 972 seasonally unforced system SIRS model with the same parameters; eigenvalues of the
 973 discrete-time SIR model were computed by numerically finding the equilibrium and
 974 calculating the Jacobian matrix.

975 **Validations for window-selection criteria**

976 We ~~use used~~ stochastic SIRS simulations to ~~validate identify optimal parameters for~~
 977 the window-selection criteria that we ~~use used~~ for the linear regression for estimating
 978 empirical resilience. For each simulation, we ~~begin began~~ by generating a random
 979 ~~intervention perturbation~~ $\alpha(t)$ from a random set of parameters. First, we ~~draw drew~~
 980 the duration of ~~intervention perturbation~~ τ_{np}_i from a uniform distribution between
 981 ~~0.5 and 3.5~~ 1 and 2 years. Then, we ~~draw drew~~ independent normal variables z_i of
 982 length $[364\tau_{\text{np}}_i]$ with a standard deviation of 0.02 and ~~take took~~ a reverse cumulative
 983 sum to obtain a realistic shape for the ~~intervention perturbation~~:

$$x_n = 1 + \sum_{i=n}^{\lfloor 364\tau_{\text{np}}_i \rfloor} z_i, \quad n = 1, \dots, \lfloor 364\tau_{\text{np}}_i \rfloor. \quad (\text{S108})$$

984 ~~We repeat~~ In contrast to simple perturbations that assume a constant reduction in
 985 transmission, this approach allows us to model transmission reduction that varies
 986 over time smoothly. We ~~repeated~~ this random generation process until less than
 987 10% of x_n exceeds 1 —this was done to ensure the perturbation term $\alpha(t)$ stays
 988 below 1 (and therefore reduce transmission) for the most part. Then, we set any
 989 values that are above 1 or below 0 ~~as to~~ 1 and 0 , respectively. Then, we randomly
 990 ~~draw drew~~ the minimum transmission during ~~intervention perturbation~~ α_{\min} from a
 991 uniform distribution between 0.5 and 0.7 and scale x_n to have a minimum of α_{\min} :

$$x_{\text{scale},n} = \alpha_{\min} + (1 - \alpha_{\min}) \times \frac{x_n - \min x_n}{1 - \min x_n}. \quad (\text{S109})$$

992 This ~~allows allowed~~ us to simulate a realistically shaped ~~interventions~~ perturbation:

$$\alpha(t) = \begin{cases} 1 & t < 2020 \\ x_{\text{scale},364(t-2020)} & 2020 \leq t < 2020 + \tau_{\text{np}}_i \\ 1 & \tau_{\text{np}}_i \leq t \end{cases} \quad (\text{S110})$$

993 Given this ~~intervention perturbation~~ function, we draw \mathcal{R}_0 from a uniform distribution
 994 between 1.5 and 3.4 and the mean duration of immunity $1/\delta$ from a uniform
 995 distribution between ~~0.5 and 2.~~ 1 and 4 . Then, we simulate the stochastic SIRS
 996 model from $S(0) = 10^8 / \mathcal{R}_0$ and $I(0) = 100$ from 1990 to 2025 and truncate the time
 997 series to 2014–2025; if the epidemic becomes extinct before the end of simulation, we
 998 discard that simulation and start over from the ~~intervention perturbation~~ generation
 999 step. ~~We then apply the window selection criteria described in the main text to~~
 1000 ~~compute the empirical resilience and compare it against the intrinsic resilience of the~~
 1001 ~~seasonally unforced system~~

1002 For each epidemic simulation, we computed the empirical resilience by varying
 1003 the threshold R for the nearest neighbor approach from 4 to 14 with increments of
 1004 2 , the number of divisions K for the window selection between 8 and 25 , and the

1005 truncation threshold a for the window selection between 1 to 3; this was done for
1006 all possible combinations of R , K , and a . We also ~~compare~~ compared this with the
1007 naive approach that uses the entire distance-from-attractor time series, starting from
1008 the maximum distance. ~~We repeat~~ to the end of the time series. ~~We repeated~~ this
1009 procedure 500 times and ~~quantify~~ quantified the correlation between empirical and
1010 intrinsic resilience estimates across two approaches.

₁₀₁₁ **Supplementary Figures**

1012 **References**

- 1013 [1] Edward A Bender, Ted J Case, and Michael E Gilpin. Perturbation experiments
1014 in community ecology: theory and practice. *Ecology*, 65(1):1–13, 1984.
- 1015 [2] Anthony R Ives and Stephen R Carpenter. Stability and diversity of ecosystems.
1016 *science*, 317(5834):58–62, 2007.
- 1017 [3] Marten Scheffer, Jordi Bascompte, William A Brock, Victor Brovkin, Stephen R
1018 Carpenter, Vasilis Dakos, Hermann Held, Egbert H Van Nes, Max Rietkerk,
1019 and George Sugihara. Early-warning signals for critical transitions. *Nature*,
1020 461(7260):53–59, 2009.
- 1021 [4] Stuart L Pimm. The structure of food webs. *Theoretical population biology*,
1022 16(2):144–158, 1979.
- 1023 [5] Michael G Neubert and Hal Caswell. Alternatives to resilience for measuring
1024 the responses of ecological systems to perturbations. *Ecology*, 78(3):653–665,
1025 1997.
- 1026 [6] Lance H Gunderson. Ecological resilience—in theory and application. *Annual
1027 review of ecology and systematics*, 31(1):425–439, 2000.
- 1028 [7] Vasilis Dakos and Sonia Kéfi. Ecological resilience: what to measure and how.
1029 *Environmental Research Letters*, 17(4):043003, 2022.
- 1030 [8] Jeanne C Chambers, Craig R Allen, and Samuel A Cushman. Operationalizing
1031 ecological resilience concepts for managing species and ecosystems at risk.
1032 *Frontiers in Ecology and Evolution*, 7:241, 2019.
- 1033 [9] Rachel E Baker, Sang Woo Park, Wenchang Yang, Gabriel A Vecchi, C Jessica E
1034 Metcalf, and Bryan T Grenfell. The impact of COVID-19 nonpharmaceutical
1035 interventions on the future dynamics of endemic infections. *Proceedings of the
1036 National Academy of Sciences*, 117(48):30547–30553, 2020.
- 1037 [10] Gabriela B Gomez, Cedric Mahé, and Sandra S Chaves. Uncertain effects of the
1038 pandemic on respiratory viruses. *Science*, 372(6546):1043–1044, 2021.
- 1039 [11] Mihaly Koltai, Fabienne Krauer, David Hodgson, Edwin van Leeuwen, Marina
1040 Treskova-Schwarzbach, Mark Jit, and Stefan Flasche. Determinants of RSV
1041 epidemiology following suppression through pandemic contact restrictions. *Epi-
1042 demics*, 40:100614, 2022.
- 1043 [12] Sang Woo Park, Brooklyn Noble, Emily Howerton, Bjarke F Nielsen, Sarah
1044 Lentz, Lilliam Ambroggio, Samuel Dominguez, Kevin Messacar, and Bryan T
1045 Grenfell. Predicting the impact of non-pharmaceutical interventions against
1046 COVID-19 on *Mycoplasma pneumoniae* in the United States. *Epidemics*,
1047 49:100808, 2024.

- 1048 [13] Eric J Chow, Timothy M Uyeki, and Helen Y Chu. The effects of the COVID-19
1049 pandemic on community respiratory virus activity. *Nature Reviews Microbiology*,
1050 21(3):195–210, 2023.
- 1051 [14] Amanda C Perofsky, Chelsea L Hansen, Roy Burstein, Shanda Boyle, Robin
1052 Prentice, Cooper Marshall, David Reinhart, Ben Capodanno, Melissa Truong,
1053 Kristen Schwabe-Fry, et al. Impacts of human mobility on the citywide trans-
1054 mission dynamics of 18 respiratory viruses in pre-and post-COVID-19 pandemic
1055 years. *Nature communications*, 15(1):4164, 2024.
- 1056 [15] Stephen M Kissler, Christine Tedijanto, Edward Goldstein, Yonatan H Grad,
1057 and Marc Lipsitch. Projecting the transmission dynamics of SARS-CoV-2
1058 through the postpandemic period. *Science*, 368(6493):860–868, 2020.
- 1059 [16] Rachel E Baker, Chadi M Saad-Roy, Sang Woo Park, Jeremy Farrar, C Jessica E
1060 Metcalf, and Bryan T Grenfell. Long-term benefits of nonpharmaceutical inter-
1061 ventions for endemic infections are shaped by respiratory pathogen dynamics.
1062 *Proceedings of the National Academy of Sciences*, 119(49):e2208895119, 2022.
- 1063 [17] Maaike C Swets, Clark D Russell, Ewen M Harrison, Annemarie B Docherty,
1064 Nazir Lone, Michelle Girvan, Hayley E Hardwick, Leonardus G Visser, Pe-
1065 ter JM Openshaw, Geert H Groeneveld, et al. SARS-CoV-2 co-infection with
1066 influenza viruses, respiratory syncytial virus, or adenoviruses. *The Lancet*,
1067 399(10334):1463–1464, 2022.
- 1068 [18] Chun-Yang Lin, Joshua Wolf, David C Brice, Yilun Sun, Macauley Locke,
1069 Sean Cherry, Ashley H Castellaw, Marie Wehenkel, Jeremy Chase Crawford,
1070 Veronika I Zarnitsyna, et al. Pre-existing humoral immunity to human common
1071 cold coronaviruses negatively impacts the protective SARS-CoV-2 antibody re-
1072 sponse. *Cell host & microbe*, 30(1):83–96, 2022.
- 1073 [19] Sam M Murray, Azim M Ansari, John Frater, Paul Klenerman, Susanna
1074 Dunachie, Eleanor Barnes, and Ane Ogbe. The impact of pre-existing cross-
1075 reactive immunity on SARS-CoV-2 infection and vaccine responses. *Nature
1076 Reviews Immunology*, 23(5):304–316, 2023.
- 1077 [20] John-Sebastian Eden, Chisha Sikazwe, Ruopeng Xie, Yi-Mo Deng, Sheena G
1078 Sullivan, Alice Michie, Avram Levy, Elena Cutmore, Christopher C Blyth,
1079 Philip N Britton, et al. Off-season RSV epidemics in Australia after easing
1080 of COVID-19 restrictions. *Nature communications*, 13(1):2884, 2022.
- 1081 [21] Georgiy V Bobashev, Stephen P Ellner, Douglas W Nychka, and Bryan T
1082 Grenfell. Reconstructing susceptible and recruitment dynamics from measles
1083 epidemic data. *Mathematical Population Studies*, 8(1):1–29, 2000.

- 1084 [22] Bärbel F Finkenstädt and Bryan T Grenfell. Time series modelling of childhood
1085 diseases: a dynamical systems approach. *Journal of the Royal Statistical Society*
1086 *Series C: Applied Statistics*, 49(2):187–205, 2000.
- 1087 [23] Floris Takens. Detecting strange attractors in turbulence. In *Dynamical Sys-*
1088 *tems and Turbulence, Warwick 1980: proceedings of a symposium held at the*
1089 *University of Warwick 1979/80*, pages 366–381. Springer, 2006.
- 1090 [24] Jonathan Dushoff, Joshua B Plotkin, Simon A Levin, and David JD Earn.
1091 Dynamical resonance can account for seasonality of influenza epidemics. *Pro-*
1092 , 101(48):16915–16916, 2004.
- 1093 [25] Alan Hastings, Carole L Hom, Stephen Ellner, Peter Turchin, and H Charles J
1094 Godfray. Chaos in ecology: is mother nature a strange attractor? *Annual review*
1095 *of ecology and systematics*, pages 1–33, 1993.
- 1096 [26] Alan Hastings, Karen C Abbott, Kim Cuddington, Tessa Francis, Gabriel Gell-
1097 ner, Ying-Cheng Lai, Andrew Morozov, Sergei Petrovskii, Katherine Scran-
1098 ton, and Mary Lou Zeeman. Transient phenomena in ecology. *Science*,
1099 361(6406):eaat6412, 2018.
- 1100 [27] Matthew B Kennel, Reggie Brown, and Henry DI Abarbanel. Determining
1101 embedding dimension for phase-space reconstruction using a geometrical con-
1102 struction. *Physical review A*, 45(6):3403, 1992.
- 1103 [28] Eugene Tan, Shannon Algar, Débora Corrêa, Michael Small, Thomas Stemler,
1104 and David Walker. Selecting embedding delays: An overview of embedding
1105 techniques and a new method using persistent homology. *Chaos: An Interdis-*
1106 *ciplinary Journal of Nonlinear Science*, 33(3), 2023.
- 1107 [29] Bjarke Frost Nielsen, Sang Woo Park, Emily Howerton, Olivia Frost Lorentzen,
1108 Mogens H Jensen, and Bryan T Grenfell. Complex multiannual cycles of My-
1109 coplasma pneumoniae: persistence and the role of stochasticity. *arXiv*, 2025.
- 1110 [30] Samantha Bosis, Susanna Esposito, HGM Niesters, GV Zuccotti, G Marseglia,
1111 Marcello Lanari, Giovanna Zuin, C Pelucchi, ADME Osterhaus, and Nicola
1112 Principi. Role of respiratory pathogens in infants hospitalized for a first episode
1113 of wheezing and their impact on recurrences. *Clinical microbiology and infection*,
1114 14(7):677–684, 2008.
- 1115 [31] Miguel L O’Ryan, Yalda Lucero, Valeria Prado, María Elena Santolaya, Marcela
1116 Rabello, Yanahara Solis, Daniela Berrios, Miguel A O’Ryan-Soriano, Hector
1117 Cortés, and Nora Mamani. Symptomatic and asymptomatic rotavirus and
1118 norovirus infections during infancy in a Chilean birth cohort. *The Pediatric*
1119 *infectious disease journal*, 28(10):879–884, 2009.

- 1120 [32] Virginia E Pitzer, Cécile Viboud, Vladimir J Alonso, Tanya Wilcox, C Jessica
1121 Metcalf, Claudia A Steiner, Amber K Haynes, and Bryan T Grenfell. Environmental drivers of the spatiotemporal dynamics of respiratory syncytial virus in
1122 the United States. *PLoS pathogens*, 11(1):e1004591, 2015.
- 1123
- 1124 [33] Arthur WD Edridge, Joanna Kaczorowska, Alexis CR Hoste, Margreet Bakker,
1125 Michelle Klein, Katherine Loens, Maarten F Jebbink, Amy Matser, Cormac M
1126 Kinsella, Paloma Rueda, et al. Seasonal coronavirus protective immunity is
1127 short-lasting. *Nature medicine*, 26(11):1691–1693, 2020.
- 1128
- 1129 [34] Samit Bhattacharyya, Per H Gesteland, Kent Korgenski, Ottar N Bjørnstad,
1130 and Frederick R Adler. Cross-immunity between strains explains the dynamical
1131 pattern of paramyxoviruses. *Proceedings of the National Academy of Sciences*,
1132 112(43):13396–13400, 2015.
- 1133
- 1134 [35] Jennifer M Radin, Anthony W Hawksworth, Peter E Kammerer, Melinda Bal-
1135 ansay, Rema Raman, Suzanne P Lindsay, and Gary T Brice. Epidemiology
1136 of pathogen-specific respiratory infections among three US populations. *PLoS
One*, 9(12):e114871, 2014.
- 1137
- 1138 [36] Guojian Lv, Limei Shi, Yi Liu, Xuecheng Sun, and Kai Mu. Epidemiological
1139 characteristics of common respiratory pathogens in children. *Scientific Reports*,
1140 14(1):16299, 2024.
- 1141
- 1142 [37] Saverio Caini, Adam Meijer, Marta C Nunes, Laetitia Henaff, Malaika Zounon,
1143 Bronke Boudewijns, Marco Del Riccio, and John Paget. Probable extinction of
1144 influenza b/yamagata and its public health implications: a systematic literature
1145 review and assessment of global surveillance databases. *The Lancet Microbe*,
1146 2024.
- 1147
- 1148 [38] Zhiyuan Chen, Joseph L-H Tsui, Bernardo Gutierrez, Simon Busch Moreno,
1149 Louis du Plessis, Xiaowei Deng, Jun Cai, Sumali Bajaj, Marc A Suchard,
1150 Oliver G Pybus, et al. COVID-19 pandemic interventions reshaped the global
1151 dispersal of seasonal influenza viruses. *Science*, 386(6722):eadq3003, 2024.
- 1152
- 1153 [39] Hai Nguyen-Tran, Sang Woo Park, Kevin Messacar, Samuel R Dominguez,
1154 Matthew R Vogt, Sallie Permar, Perdita Permaul, Michelle Hernandez, Daniel C
1155 Douek, Adrian B McDermott, et al. Enterovirus D68: a test case for the use of
1156 immunological surveillance to develop tools to mitigate the pandemic potential
1157 of emerging pathogens. *The Lancet Microbe*, 3(2):e83–e85, 2022.
- 1158
- 1159 [40] Bryan T Grenfell, Ottar N Bjørnstad, and Bärbel F Finkenstädt. Dynamics of
1160 measles epidemics: scaling noise, determinism, and predictability with the TSIR
1161 model. *Ecological monographs*, 72(2):185–202, 2002.
- 1162

- 1156 [41] Katharine R Dean, Fabienne Krauer, Lars Walløe, Ole Christian Lingjærde, Bar-
1157 bara Bramanti, Nils Chr Stenseth, and Boris V Schmid. Human ectoparasites
1158 and the spread of plague in Europe during the Second Pandemic. *Proceedings*
1159 *of the National Academy of Sciences*, 115(6):1304–1309, 2018.
- 1160 [42] Margarita Pons-Salort and Nicholas C Grassly. Serotype-specific immunity
1161 explains the incidence of diseases caused by human enteroviruses. *Science*,
1162 361(6404):800–803, 2018.
- 1163 [43] Sarah Cobey and Edward B Baskerville. Limits to causal inference with state-
1164 space reconstruction for infectious disease. *PLoS one*, 11(12):e0169050, 2016.
- 1165 [44] P Rohani, CJ Green, NB Mantilla-Beniers, and Bryan T Grenfell. Ecological
1166 interference between fatal diseases. *Nature*, 422(6934):885–888, 2003.
- 1167 [45] Sema Nickbakhsh, Colette Mair, Louise Matthews, Richard Reeve, Paul CD
1168 Johnson, Fiona Thorburn, Beatrix Von Wissmann, Arlene Reynolds, James
1169 McMenamin, Rory N Gunson, et al. Virus–virus interactions impact the popu-
1170 lation dynamics of influenza and the common cold. *Proceedings of the National*
1171 *Academy of Sciences*, 116(52):27142–27150, 2019.
- 1172 [46] Neil Ferguson, Roy Anderson, and Sunetra Gupta. The effect of antibody-
1173 dependent enhancement on the transmission dynamics and persistence of
1174 multiple-strain pathogens. *Proceedings of the National Academy of Sciences*,
1175 96(2):790–794, 1999.
- 1176 [47] Public Health Agency of Canada. Respiratory virus detections in
1177 Canada. 2024. <https://www.canada.ca/en/public-health/services/surveillance/respiratory-virus-detections-canada.html>. Accessed Sep
1178 4, 2024.
- 1180 [48] Centre for Health Protection. Detection of pathogens from respiratory spec-
1181 imens. 2024. <https://www.chp.gov.hk/en/statistics/data/10/641/642/2274.html>. Accessed Nov 20, 2024.
- 1183 [49] Centre for Health Protection. Detection of gastroenteritis viruses from faecal
1184 specimens. 2024. <https://www.chp.gov.hk/en/statistics/data/10/641/717/3957.html>. Accessed Nov 20, 2024.
- 1186 [50] Korea Disease Control and Prevention Agency. Acute respiratory infection,
1187 Sentinel surveillance infectious diseases. 2024. <https://dportal.kdca.go.kr/pot/is/st/ari.do>. Accessed Nov 20, 2024.
- 1189 [51] Edward Goldstein, Sarah Cobey, Saki Takahashi, Joel C Miller, and Marc Lipsitch.
1190 Predicting the epidemic sizes of influenza A/H1N1, A/H3N2, and B: a
1191 statistical method. *PLoS medicine*, 8(7):e1001051, 2011.

- 1192 [52] Karline Soetaert, Thomas Petzoldt, and R Woodrow Setzer. Solving differential
1193 equations in R: package deSolve. *Journal of statistical software*, 33:1–25, 2010.
- 1194 [53] R Core Team. *R: A Language and Environment for Statistical Computing*. R
1195 Foundation for Statistical Computing, Vienna, Austria, 2023.
- 1196 [54] Sang Woo Park, Inga Holmdahl, Emily Howerton, Wenchang Yang, Rachel E
1197 Baker, Gabriel A Vecchi, Sarah Cobey, C Jessica E Metcalf, and Bryan T Gren-
1198 fell. Interplay between climate, childhood mixing, and population-level suscep-
1199 tibility explains a sudden shift in RSV seasonality in Japan. *medRxiv*, pages
1200 2025–03, 2025.
- 1201 [55] Bob Carpenter, Andrew Gelman, Matthew D Hoffman, Daniel Lee, Ben
1202 Goodrich, Michael Betancourt, Marcus A Brubaker, Jiqiang Guo, Peter Li,
1203 and Allen Riddell. Stan: A probabilistic programming language. *Journal of
1204 statistical software*, 76, 2017.
- 1205 [56] Stan Development Team. RStan: the R interface to Stan, 2024. R package
1206 version 2.32.6.

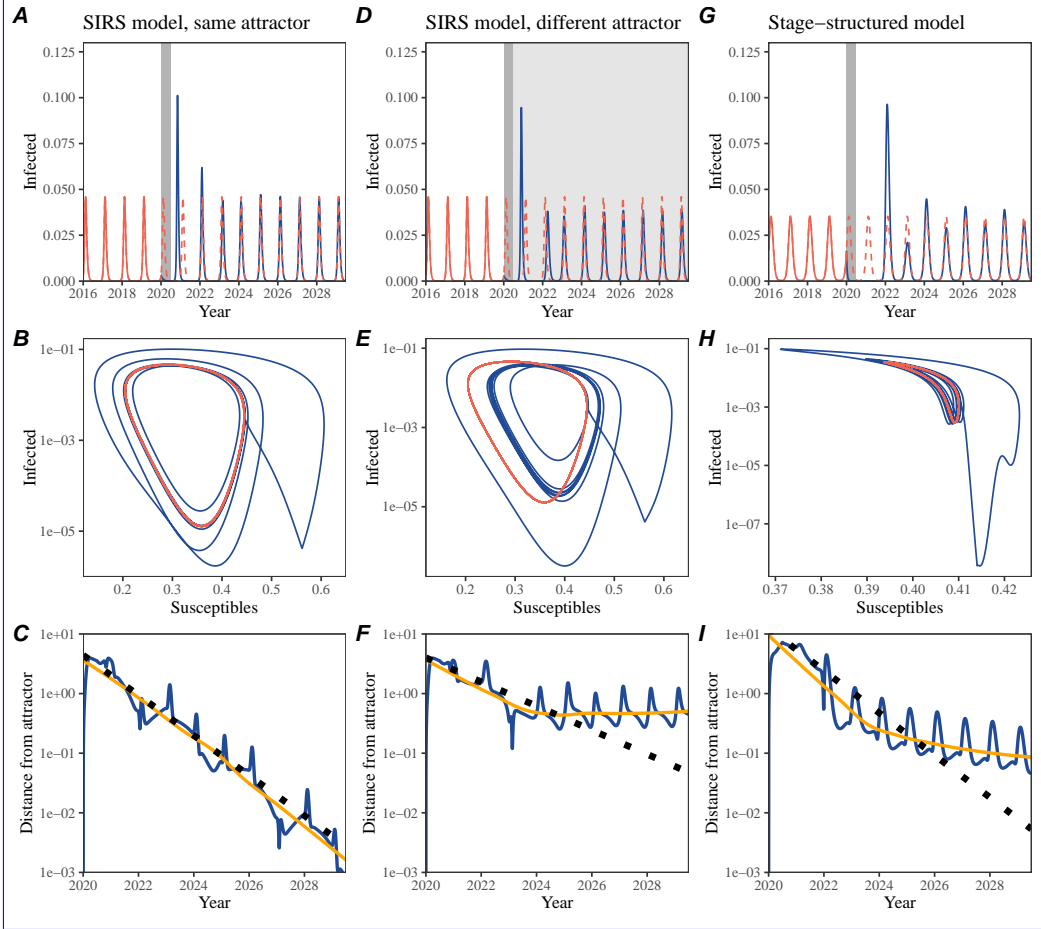


Figure 2: **Conceptual framework for measuring pathogen resilience following NPIs across different scenarios. A simple method to measure pathogen resilience following pandemic perturbations across different scenarios.** (A, D, G) Simulated epidemic trajectories across various models. Red and blue solid lines represent epidemic dynamics before and after **interventions**. Red dashed lines represent counterfactual epidemic dynamics in the absence of **interventions**. Gray regions indicate the duration of **interventions**, with the dark gray region representing a 50% transmission reduction and the light gray region representing a 10% transmission reduction. (B, E, H) Phase plane representation of the time series in panels A, D, and G alongside the corresponding **model** susceptible host dynamics. Red and blue solid lines represent epidemic trajectories on an SI phase plane before and after **interventions**. (C, F, I) Changes in **logged**-distance from the attractor over time on a **log scale**. Blue lines represent the **logged**-distance from the attractor. Orange lines represent the locally estimated scatterplot smoothing (LOESS) fits to the logged distance from the attractor. Dotted lines are superimposed as a comparison to have shown the same slope as the intrinsic resilience of the seasonally unforced system.

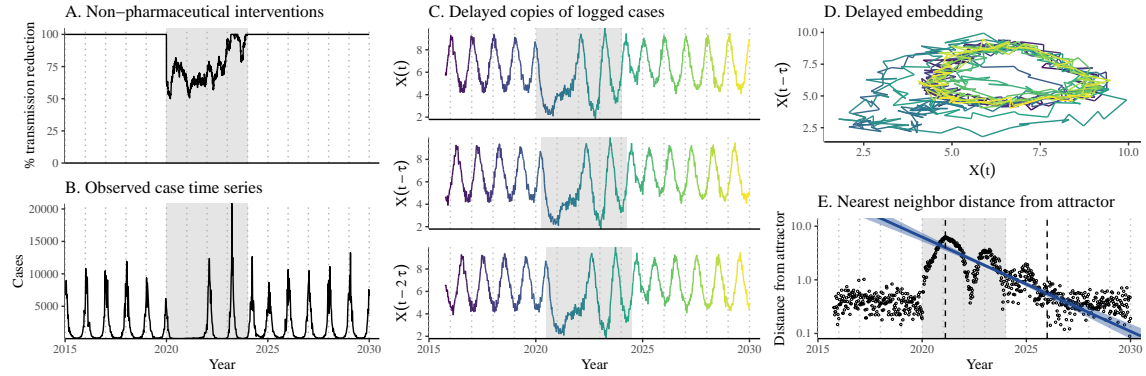


Figure 3: **A schematic diagram explaining how pathogen resilience can be inferred from real data. A schematic diagram explaining the inference of pathogen resilience from synthetic data.** (A) A realistic example of a synthetic NPI simulated pandemic perturbation, represented by a relative reduction in transmission. (B) The impact of the synthetic NPI pandemic perturbation on epidemic dynamics simulated using a stochastic SIRS model with demographic stochasticity. (C) Generating delayed copies of the logged time series allows us to obtain an embedding. (D) Two dimensional representation of an embedding. (E) Delayed embedding allows us to calculate the nearest neighbor distance from the empirical attractor, which is determined based on the pre-pandemic time series. Blue lines and dashed regions represent the linear regression fit and the associated 95% confidence interval. This distance time series can be used to infer pathogen resilience by fitting a linear regression after choosing an appropriate window for linear regression. For illustration purposes, an arbitrary fitting window was chosen.

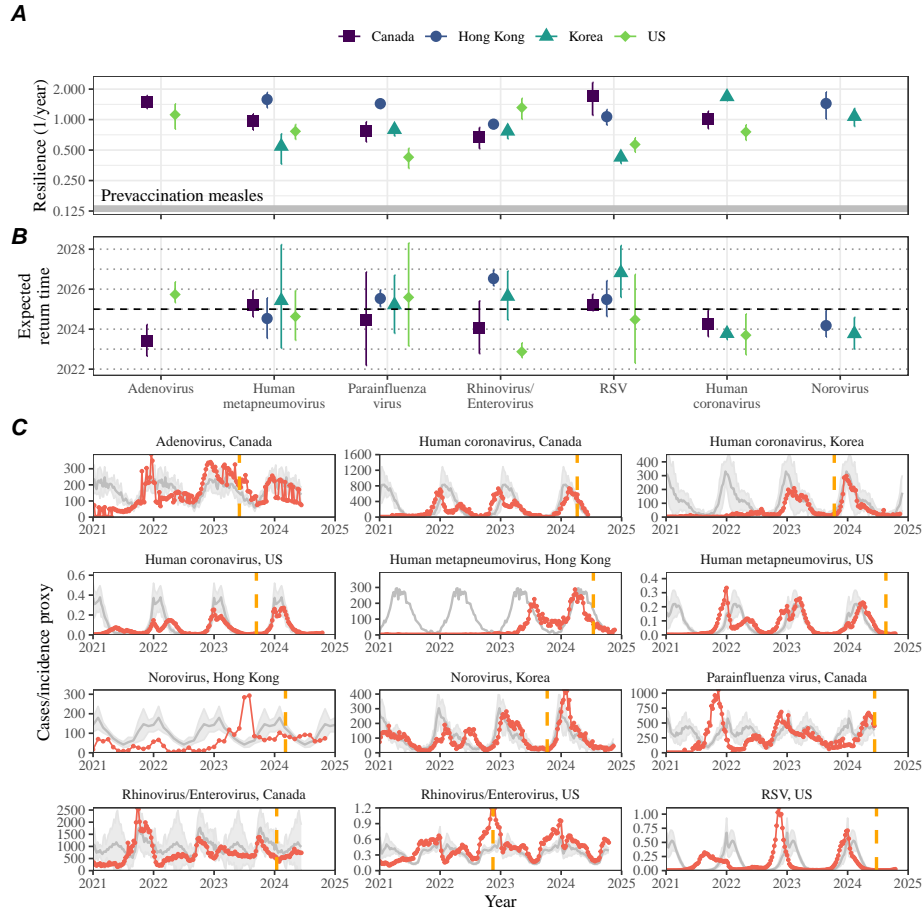


Figure 4: **Summary of resilience estimates.** **Summary of resilience estimates and predictions for return time.** (A) Estimated pathogen resilience. The gray horizontal line represents the intrinsic resilience of pre-vaccination measles dynamics. (B) Predicted timing of when each pathogen will return to their pre-pandemic cycles. The dashed line in panel B indicates the end of **2024 (current observation time).** Error bars represent 95% confidence intervals. (C) Observed dynamics for pathogen that are predicted to have returned before the end of 2024. Red points and lines represent data before 2020. Gray lines and shaded regions represent the mean seasonal patterns and corresponding 95% confidence intervals around the mean, previously shown in Figure 1. Orange vertical lines represent the predicted timing of return.

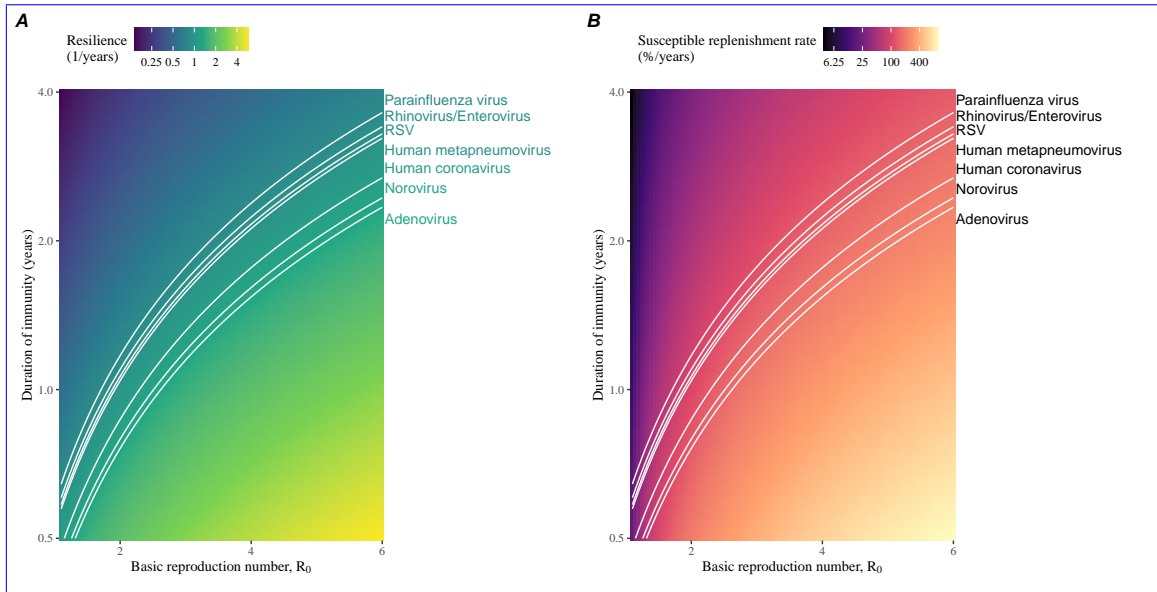


Figure 5: **Linking pathogen resilience to epidemiological parameters and susceptible host dynamics.** (A) ~~The heat map represents intrinsic~~ Intrinsic resilience as a function of the basic reproduction number \mathcal{R}_0 and the duration of immunity. (B) ~~The heat map represents per-capita~~ Per-capita susceptible replenishment rate as a function of the basic reproduction number \mathcal{R}_0 and the duration of immunity. The standard SIRS model ~~without seasonal forcing~~ is used to compute intrinsic resilience and ~~the~~ per-capita susceptible replenishment rate. Lines correspond to a set of parameters that are consistent with mean resilience estimates for each pathogen. ~~Pathogens are ranked based on their mean resilience estimates~~, averaged across different countries.

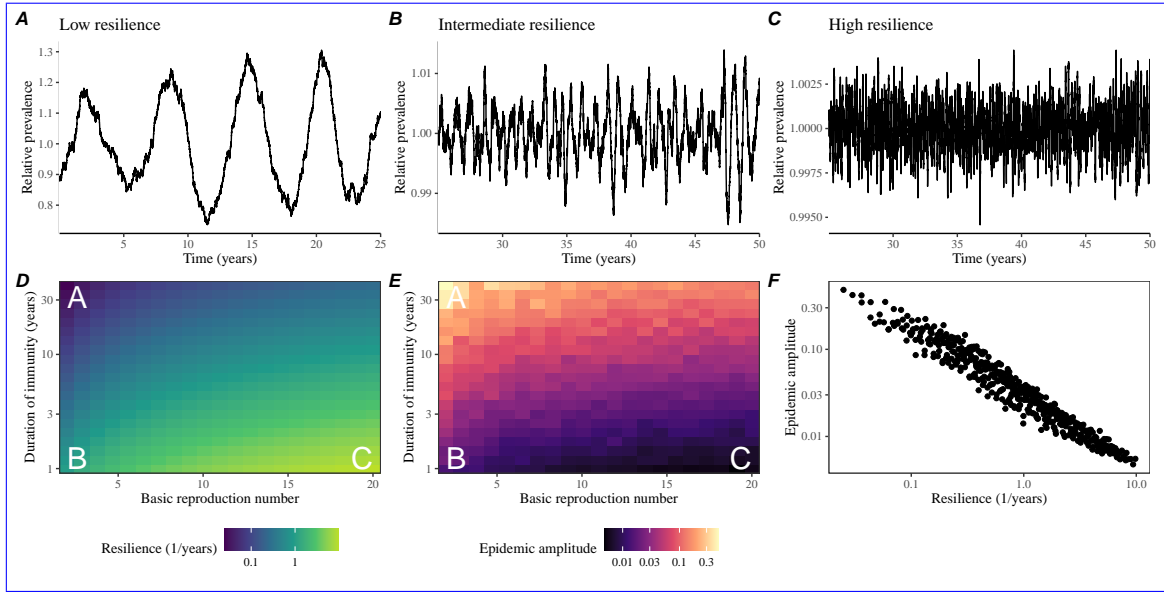


Figure 6: **Linking resilience of a host-pathogen system to its sensitivity to stochastic perturbations.** (A–C) Epidemic trajectories of a stochastic SIRS model across three different resilience values: low, intermediate, and high. The relative prevalence was calculated by dividing infection prevalence by its mean value. (D) Intrinsic resilience of a system as a function of the basic reproduction number \mathcal{R}_0 and the duration of immunity. (E) Epidemic amplitude as a function of the basic reproduction number \mathcal{R}_0 and the duration of immunity. The epidemic amplitude corresponds to $(\max I - \min I)/(2\bar{I})$, where \bar{I} represents the mean prevalence. Labels A–C in panels D and E correspond to scenarios shown in panels A–C. (F) The relationship between pathogen resilience and epidemic amplitude.

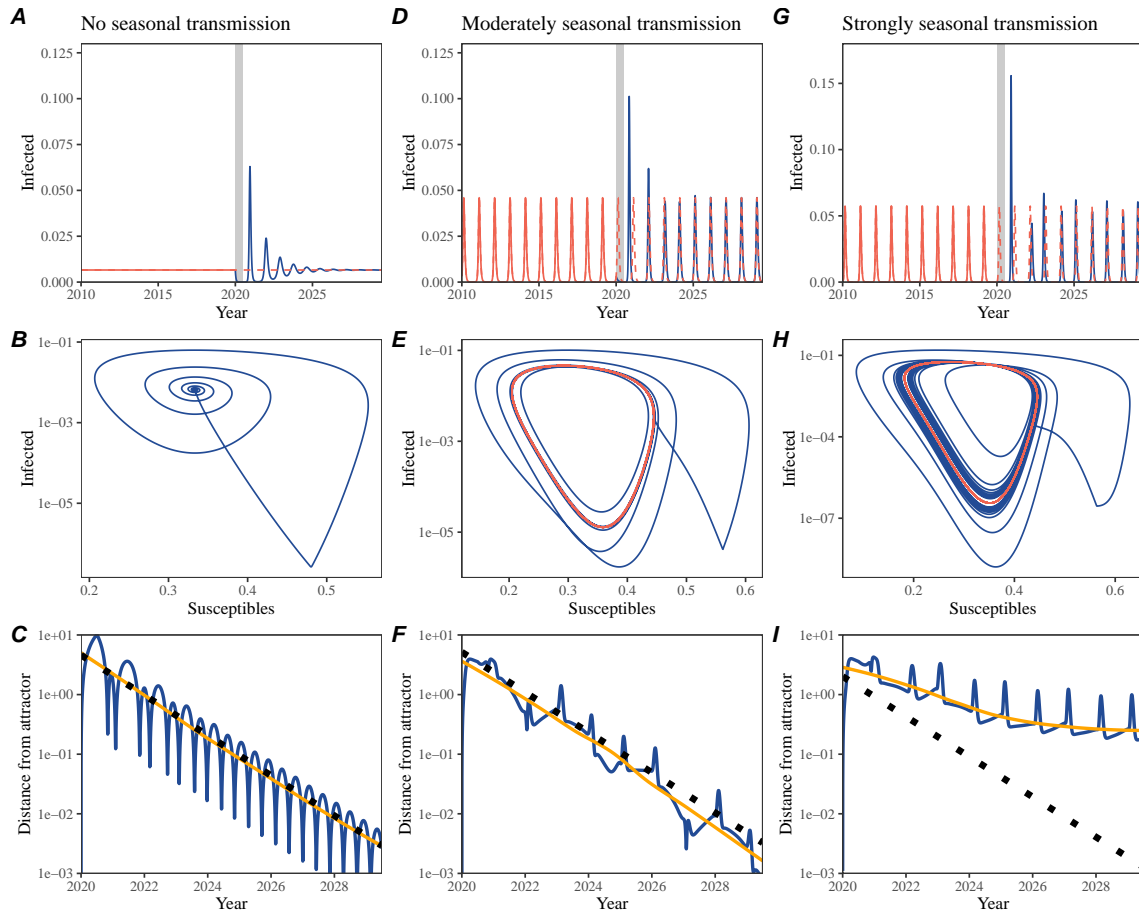


Figure S1: Impact of seasonal transmission on pathogen resilience. (A, D, G) Simulated epidemic trajectories using the SIRS model without seasonal forcing (A), with seasonal forcing of amplitude of 0.2 (D), and with seasonal forcing of amplitude of 0.2 (G). Red and blue solid lines represent epidemic dynamics before and after interventions are introduced, respectively. Red dashed lines represent counterfactual epidemic dynamics in the absence of interventions. Gray regions indicate the duration of interventions. (B, E, H) Phase plane representation of the time series in panels A, D, and G alongside the corresponding model susceptible host dynamics. Red and blue solid lines represent epidemic trajectories on an SI phase plane before and after interventions are introduced, respectively. (C, F, I) Changes in logged distance from the attractor over time. Blue lines represent the logged distance from the attractor. Orange lines represent the locally estimated scatterplot smoothing (LOESS) fits to the logged distance from the attractor. Dotted lines are superimposed as a comparison to have show the same slope as the intrinsic resilience of the seasonally unforced system.

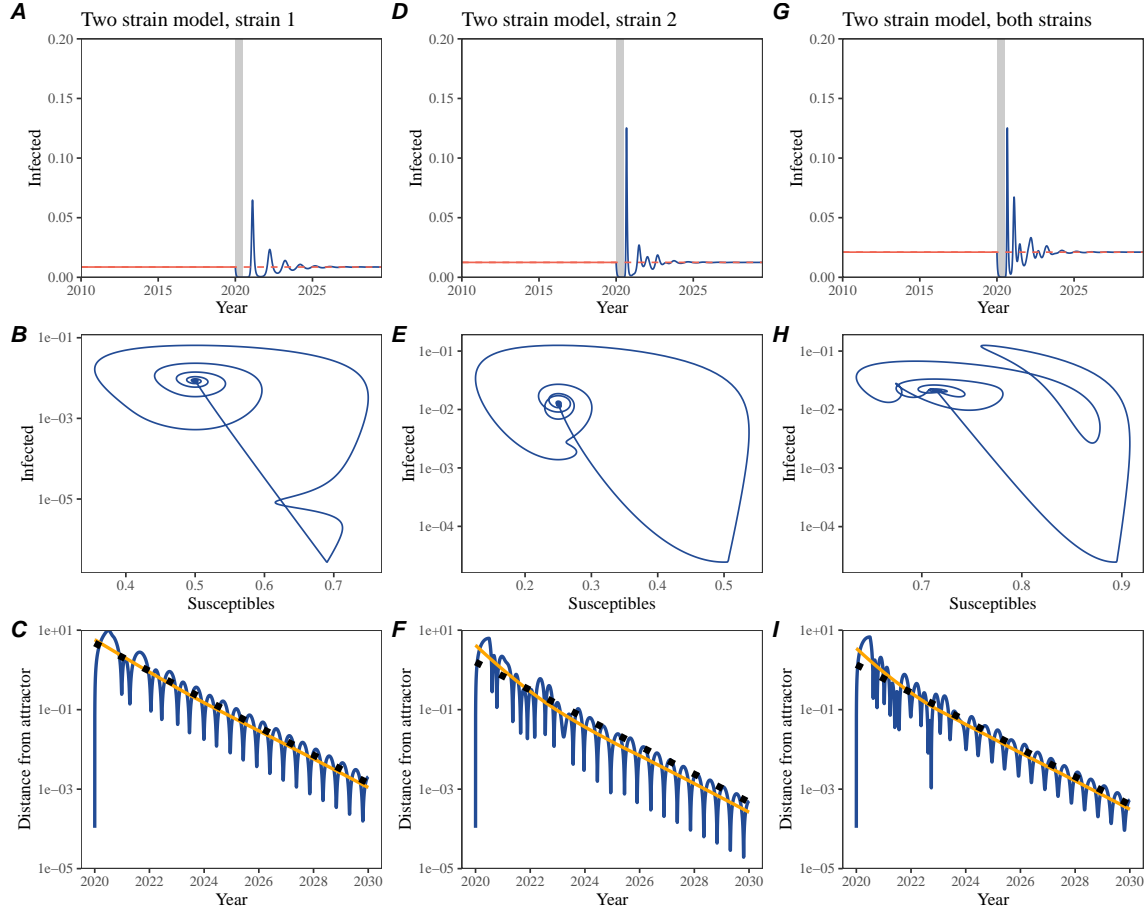


Figure S2: **Conceptual framework for measuring pathogen resilience following NPIs for a multi-strain system without seasonal forcing.** A simple method to measure pathogen resilience following pandemic perturbations for a two-strain competition system without seasonal forcing. (A, D, G) Simulated epidemic trajectories using a multi-strain-two-strain system without seasonal forcing. In this model, two strains compete through cross immunity. Red and blue solid lines represent epidemic dynamics before and after interventions are introduced, respectively. Red dashed lines represent counterfactual epidemic dynamics in the absence of interventions. Gray regions indicate the duration of interventions. (B, E, H) Phase plane representation of the time series in panels A, D, and G alongside the corresponding modelsusceptible host dynamics. Red and blue solid lines represent epidemic trajectories on an SI phase plane before and after interventions are introduced, respectively. (C, F, I) Changes in logged distance from the attractor over time. Blue lines represent the logged distance from the attractor. Orange lines represent the locally estimated scatterplot smoothing (LOESS) fits to the logged distance from the attractor. Dotted lines are superimposed as a comparison to have shown the same slope as the intrinsic resilience of the seasonally unforced system.

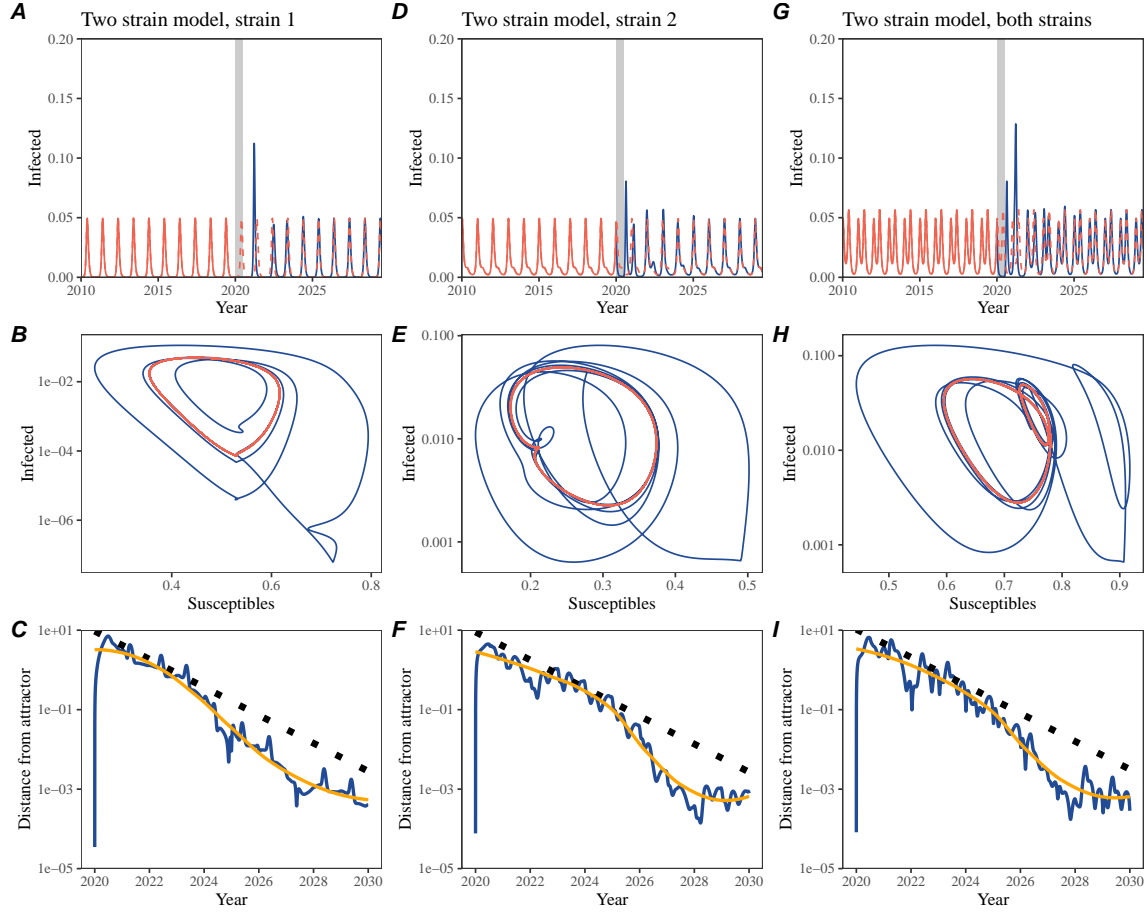


Figure S3: Conceptual framework for measuring pathogen resilience following NPIs for a multi-strain system with seasonal forcing. A simple method to measure pathogen resilience following pandemic perturbations for a two-strain competition system with seasonal forcing. (A, D, G) Simulated epidemic trajectories using a multi-strain two-strain system with seasonal forcing (amplitude of 0.2). In this model, two strains compete through cross immunity. Red and blue solid lines represent epidemic dynamics before and after interventions are introduced, respectively. Red dashed lines represent counterfactual epidemic dynamics in the absence of interventions. Gray regions indicate the duration of interventions. (B, E, H) Phase plane representation of the time series in panels A, D, and G alongside the corresponding modelsusceptible host dynamics. Red and blue solid lines represent epidemic trajectories on an SI phase plane before and after interventions are introduced, respectively. (C, F, I) Changes in logged distance from the attractor over time. Blue lines represent the logged distance from the attractor. Orange lines represent the locally estimated scatterplot smoothing (LOESS) fits to the logged distance from the attractor. Dotted lines are superimposed as a comparison to have shown the same slope as the intrinsic resilience of the seasonally unforced system.

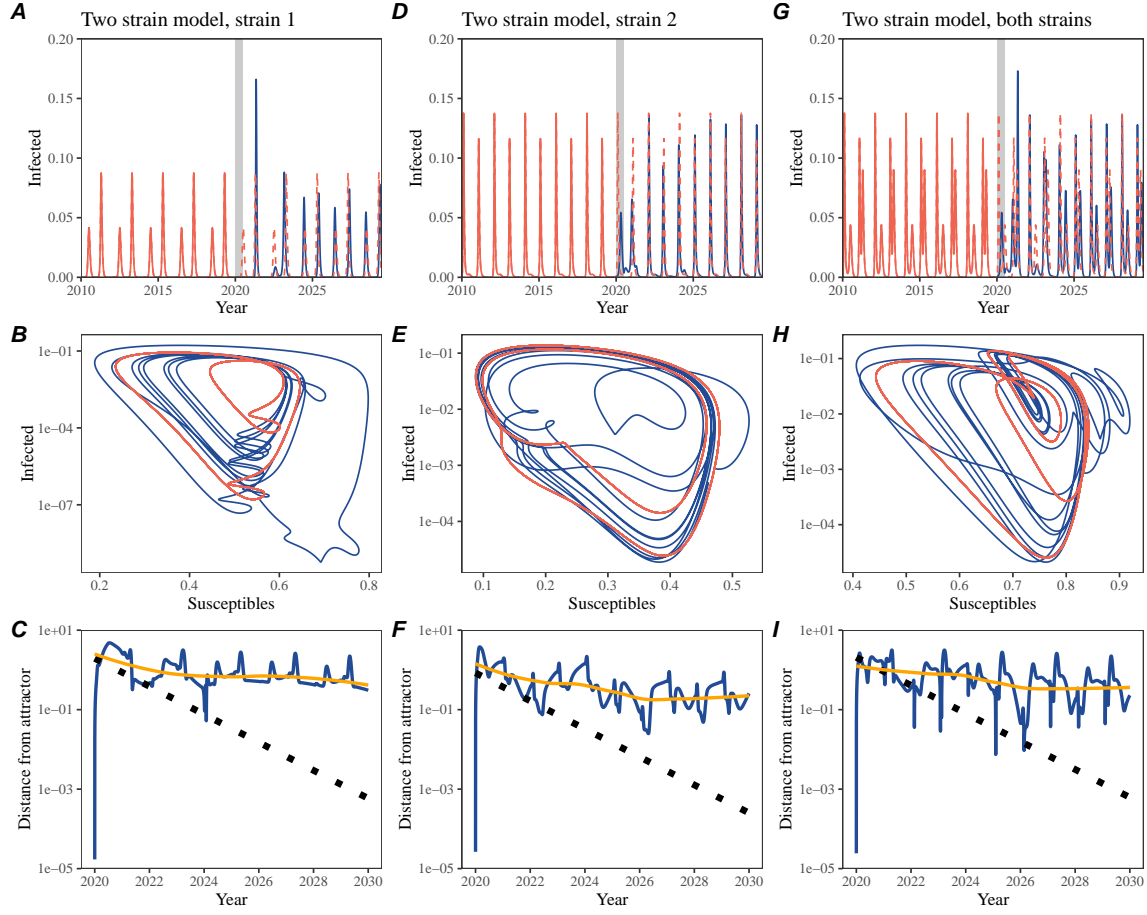


Figure S4: **Conceptual framework for measuring pathogen resilience following NPIs for a multi-strain system with strong seasonal forcing.** **A simple method to measure pathogen resilience following pandemic perturbations for a multi-strain competition system with strong seasonal forcing.** (A, D, G) Simulated epidemic trajectories using a ~~multi-strain~~ two-strain system with seasonal forcing (amplitude of ~~0.40.2~~). In this model, two strains compete through cross immunity. Red and blue solid lines represent epidemic dynamics before and after interventions are introduced, respectively. Red dashed lines represent counterfactual epidemic dynamics in the absence of interventions. Gray regions indicate the duration of interventions. (B, E, H) Phase plane representation of the time series in panels A, D, and G alongside the corresponding modelsusceptible host dynamics. Red and blue solid lines represent epidemic trajectories on an SI phase plane before and after interventions are introduced, respectively. (C, F, I) Changes in logged distance from the attractor over time. Blue lines represent the logged distance from the attractor. Orange lines represent the locally estimated scatterplot smoothing (LOESS) fits to the logged distance from the attractor. Dotted lines are superimposed as a comparison to have shown the same slope as the intrinsic resilience of the seasonally unforced system.

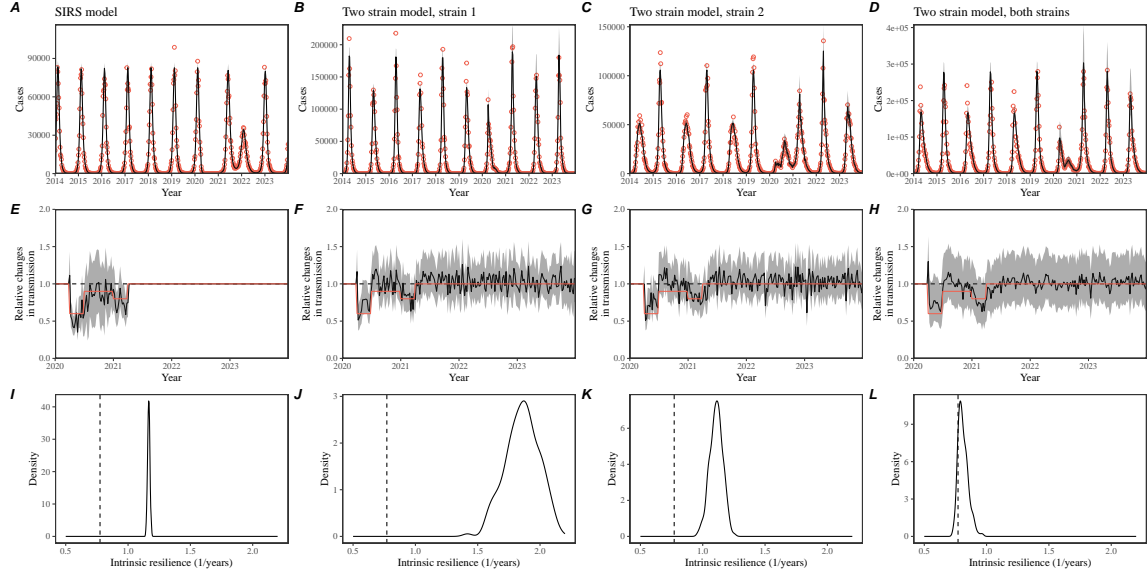


Figure S5: Mechanistic model fits to simulated data and inferred intrinsic resilience. We simulated discrete time, stochastic epidemic trajectories using a seasonally forced SIRS model (A, D–E, G–I) and a seasonally forced two-strain model (B–D, J–F–H, and J–L) and tested whether we can estimate the intrinsic resilience of the seasonally unforced versions of the model by fitting a mechanistic model (Supplementary Text). We fitted the same discrete time, one strain, deterministic SIRS model in each scenario. (A–D) Simulated case time series from corresponding models shown in the title (red) and SIRS model fits (black). (B, E, H, K–E–H) Assumed changes in transmission due to COVID-19 interventions pandemic perturbations (red) and estimated changes time-varying relative transmission rates for the perturbation impact from the SIRS model fits (black). Solid lines and shaded regions represent fitted posterior median and 95% credible intervals. (C, F, I, L I–L) True Comparisons between the true and estimated intrinsic resilience of the seasonally unforced system (vertical). Vertical lines and represent the true intrinsic resilience of the seasonally unforced system. Density plots represent the posterior distribution of the inferred intrinsic resilience from of the seasonally unforced SIRS model (density plots) using fitted parameters.

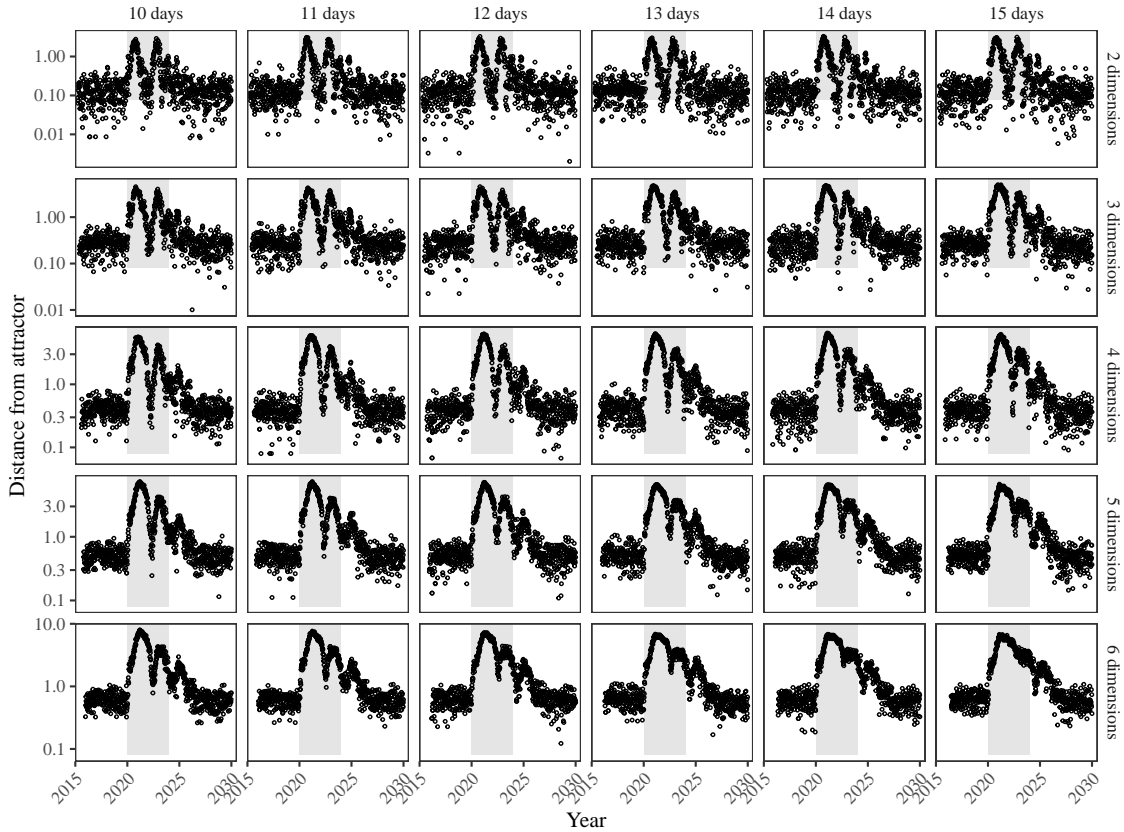


Figure S6: ~~Sensitivity of the distance from attractor to choices about embedding lags and dimensions.~~ Sensitivity of the distance from the attractor to choice of embedding lags and dimensions. Sensitivity analysis for the distance-from-attractor time series shown in Figure 3E in the main text by varying the embedding lag between 10–15 days and embedding dimensions between 2–6 dimensions. ~~The gray region represents the assumed period of pandemic perturbation.~~

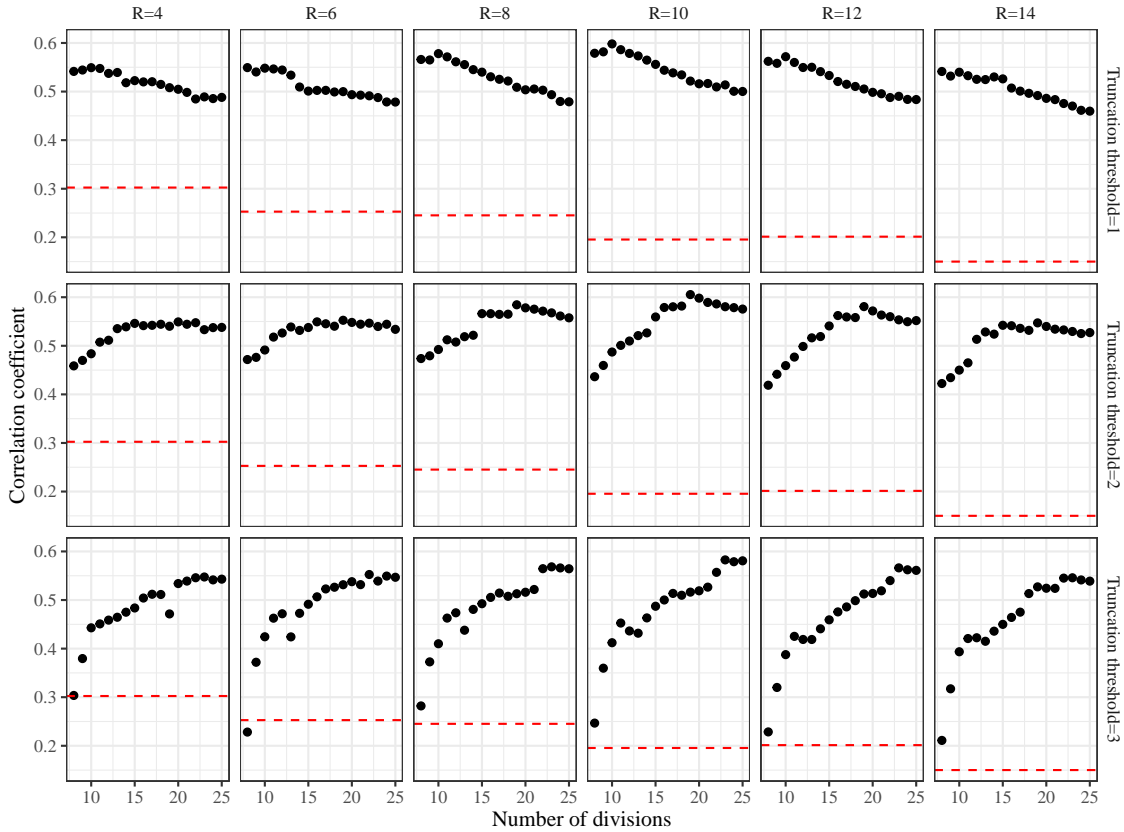


Figure S7: **Impact of fitting window selection on the estimation of empirical resilience.** We simulated 500 epidemics using a stochastic SIRS model with randomly drawn parameters and randomly generated intervention impacts on pandemic perturbations (Supplementary Text). For each simulation, we reconstructed the false nearest neighbor threshold R for reconstructing the empirical attractor based on the approach outlined in Figure 3 parameters for regression window selection (i.e., the truncation threshold a and estimate the distance from attractor number of divisions K). The Each point represents the resulting correlation coefficient between empirical and intrinsic resilience estimates for a given scenario. Dashed lines represent the correlation coefficient between empirical and intrinsic resilience estimates for the naive approach that fits a linear regression on a log scale, starting from the maximum distance until the end of the time series. The window-based approach tries to select an appropriate window by smoothing the distance estimates and finding a time period when the smoothed time series crosses pre-determined threshold, relatively to the maximum distance; then, a linear regression is fitted by using the raw distance within this time period.

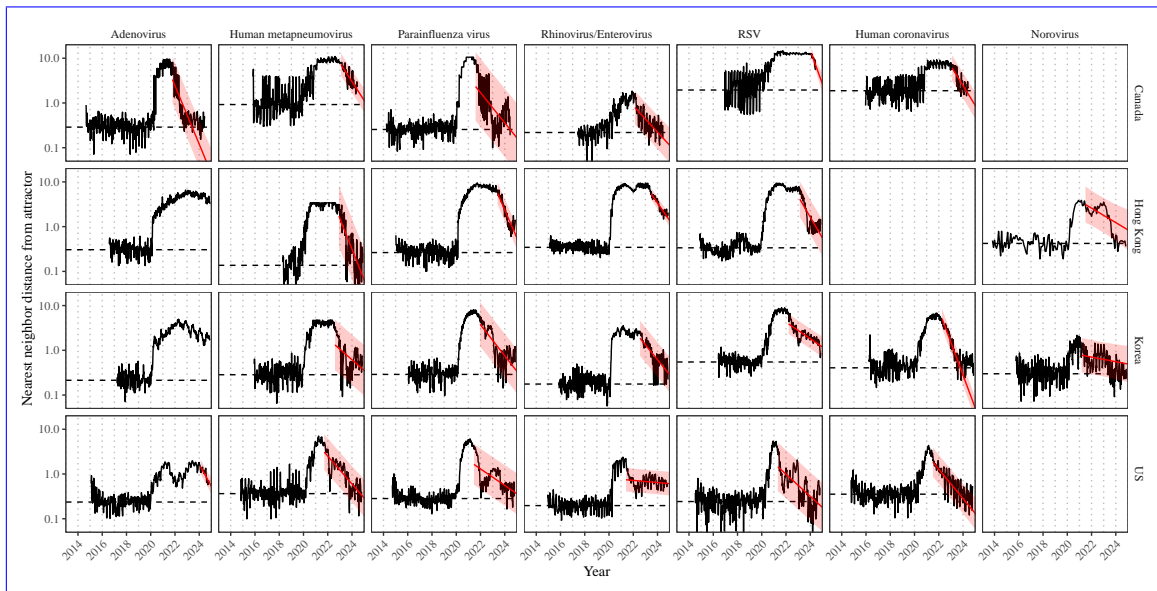


Figure S8: **Estimated time series of distance from the attractor for each pathogen and corresponding linear regression fits using automated window selection criterion across Canada, Hong Kong, Korea, and the US.** Black lines represent the estimated distance from the attractor. Red lines and shaded regions represent the linear regression fits and corresponding 95% confidence intervals. Dashed lines represent the average of the pre-pandemic nearest neighbor distances.

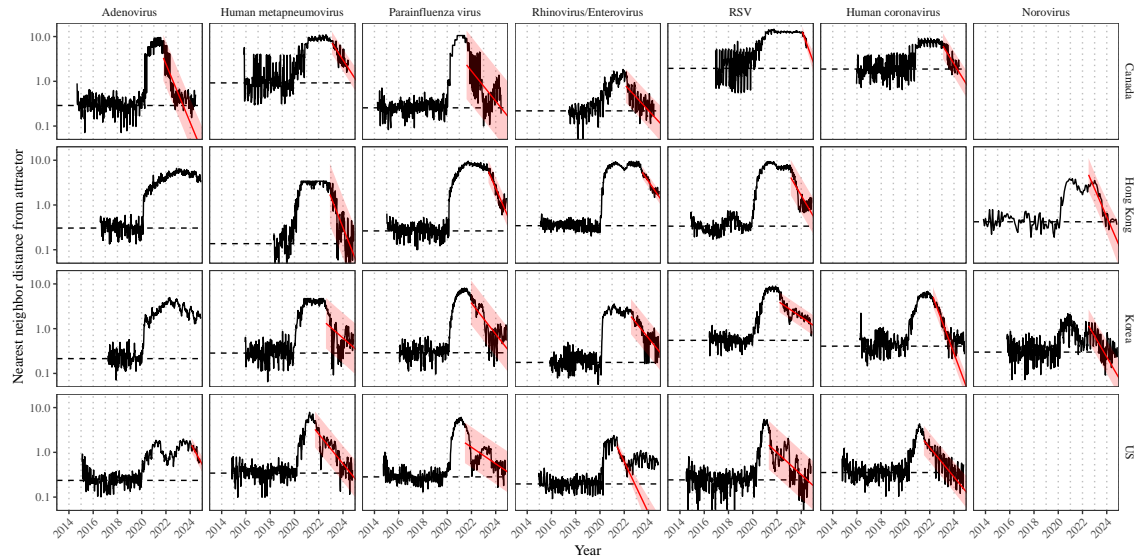
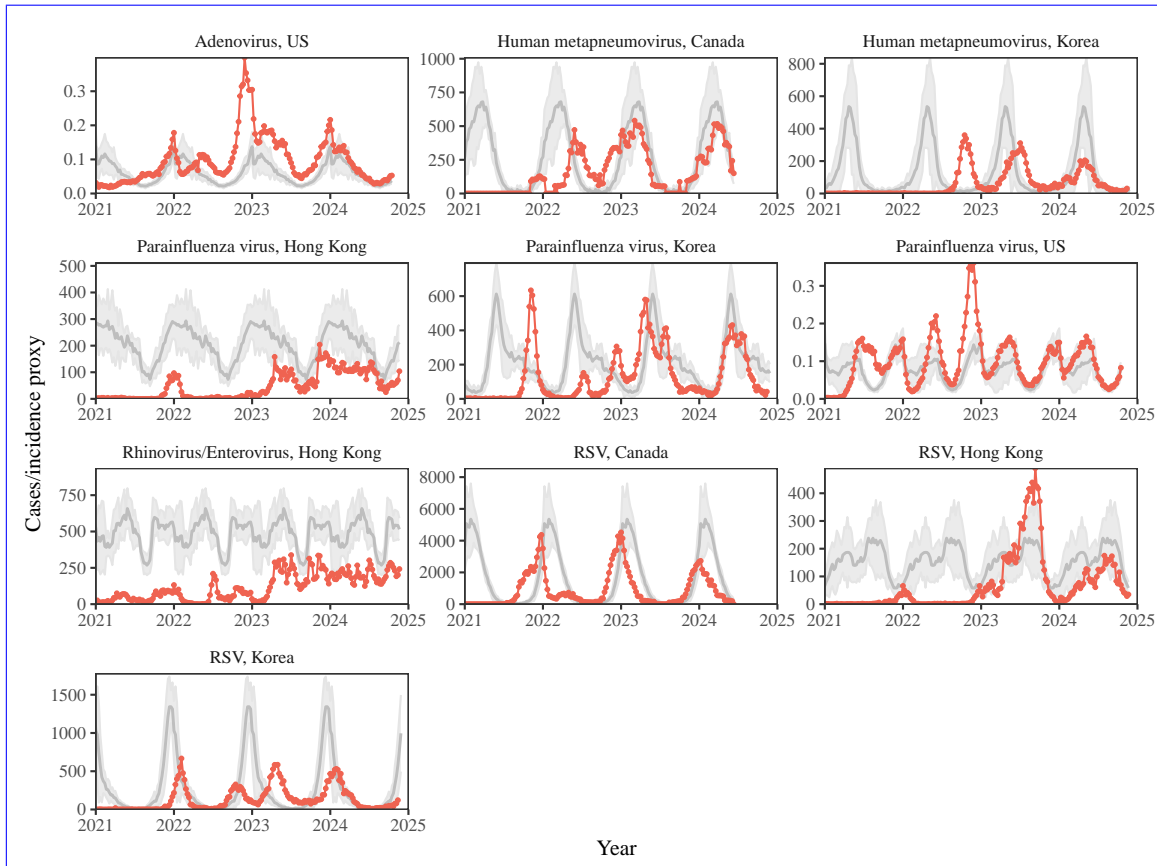


Figure S9: **Estimated time series of distance from attractor for each pathogen across Canada, Hong Kong, Korea, and the US.** Estimated time series of distance from the attractor for each pathogen and corresponding linear regression fits across Canada, Hong Kong, Korea, and the US, including ad-hoc regression window selection. We used ad-hoc regression windows for norovirus in Hong Kong and Korea and rhinovirus/enterovirus in the US. Black lines represent the estimated distance from the attractor. Red lines and shaded regions represent the linear regression fits and corresponding 95% confidence intervals. Dashed lines represent the average of the pre-pandemic nearest neighbor distances.



Estimated time series of distance from attractor for each pathogen across Canada, Hong Kong, Korea, and the US using higher embedding dimensions. Black Observed dynamics for pathogen that are predicted to return after the end of 2024. Red points and lines represent the estimated distance from attractor. Red data before 2020. Gray lines and shaded regions represent the linear regression fits mean seasonal patterns and corresponding 95% confidence intervals . Dashed lines represent around the average of the pre-pandemic nearest neighbor distances. A lower mean, previously shown in Figure 1.

Estimated time series of distance from attractor for each pathogen across Canada, Hong Kong, Korea, and the US using higher embedding dimensions. Black Observed dynamics for pathogen that are predicted to return after the end of 2024. Red points and lines represent the estimated distance from attractor. Red data before 2020. Gray lines and shaded regions represent the linear regression fits mean seasonal patterns and corresponding 95% confidence intervals . Dashed lines represent around the average of the pre-pandemic nearest neighbor distances. A lower mean, previously shown in Figure 1.

Figure S10: Predicted timing of when each pathogen will return to their pre-pandemic cycles (zoomed out). The dashed line in panel B indicates the end of 2024 (current observation time). Error bars represent 95% confidence intervals. Estimated time series of distance from attractor for each pathogen across Canada, Hong Kong, Korea, and the US using higher embedding dimensions. Black Observed dynamics for pathogen that are predicted to return after the end of 2024. Red points and lines represent the estimated distance from attractor. Red data before 2020. Gray lines and shaded regions represent the linear regression fits mean seasonal patterns and corresponding 95% confidence intervals . Dashed lines represent around the average of the pre-pandemic nearest neighbor distances. A lower mean, previously shown in Figure 1.

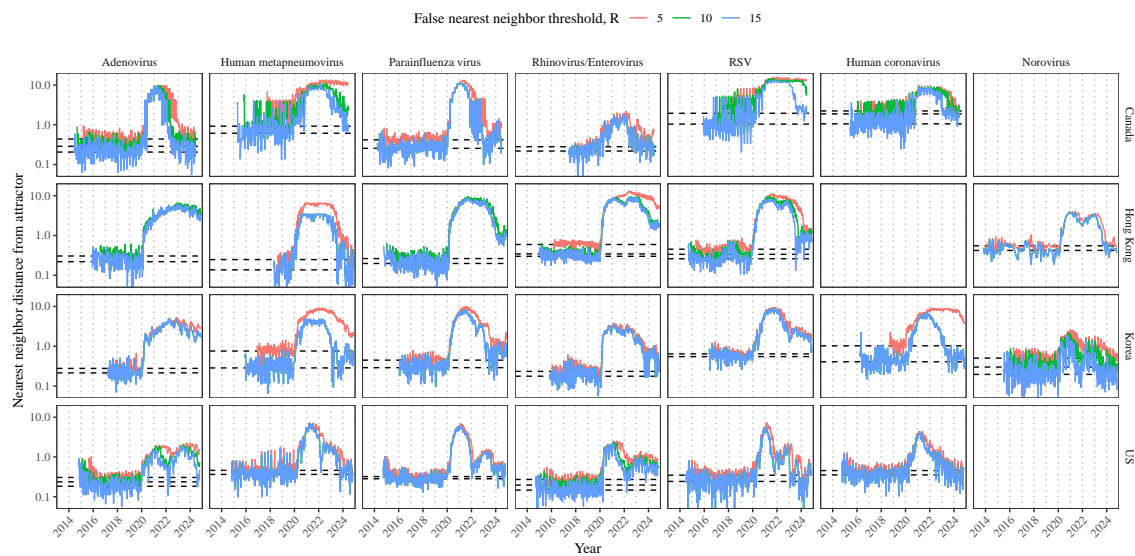


Figure S11: Estimated time series of distance from the attractor for each pathogen across different choices about false nearest neighbor threshold values. Using higher threshold is used values for determining embedding dimensions with the false nearest neighbors neighbor approach , thereby yielding a higher gives lower embedding dimension dimensions. Colored lines represent the estimated distance from the attractor for different threshold values.

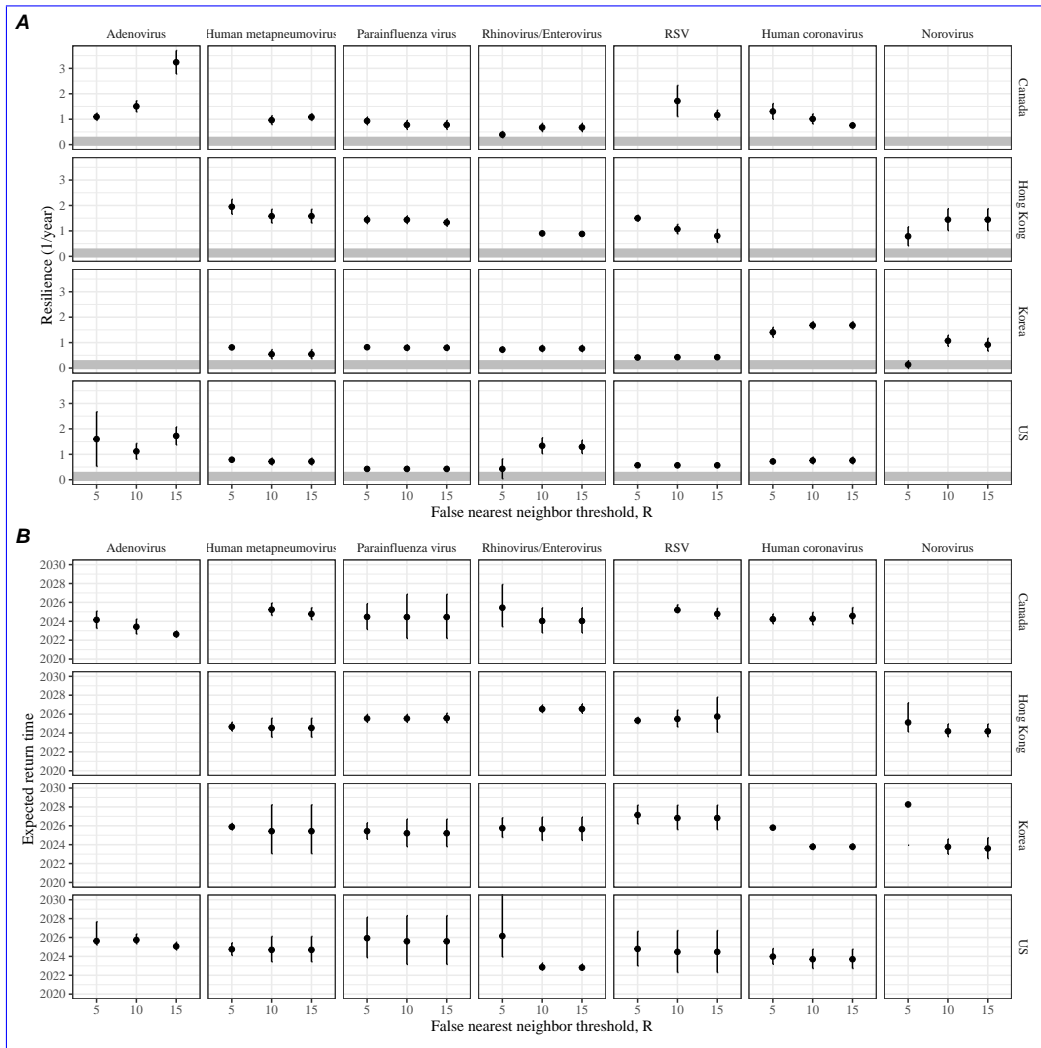


Figure S12: **Summary of resilience estimates using higher embedding dimensions.** **Summary of resilience estimates and predictions for return time across different choices about false nearest neighbor threshold values.** The automated window selection method was used for all scenarios to estimate pathogen resilience, except for norovirus in Hong Kong and Korea and rhinovirus/enterovirus in the US. We used the same ad-hoc regression windows for norovirus in Hong Kong and Korea and rhinovirus/enterovirus in the US as we did in the main analysis. (A) Estimated pathogen resilience. The gray horizontal line represents the intrinsic resilience of pre-vaccination measles dynamics. (B) Predicted timing of when each pathogen will return to their pre-pandemic cycles. The dashed line in panel B indicates the end of 2024 (current observation time). Error bars represent 95% confidence intervals. **A lower threshold is used for determining embedding dimensions with the false nearest neighbors approach, thereby yielding a higher embedding dimension.**

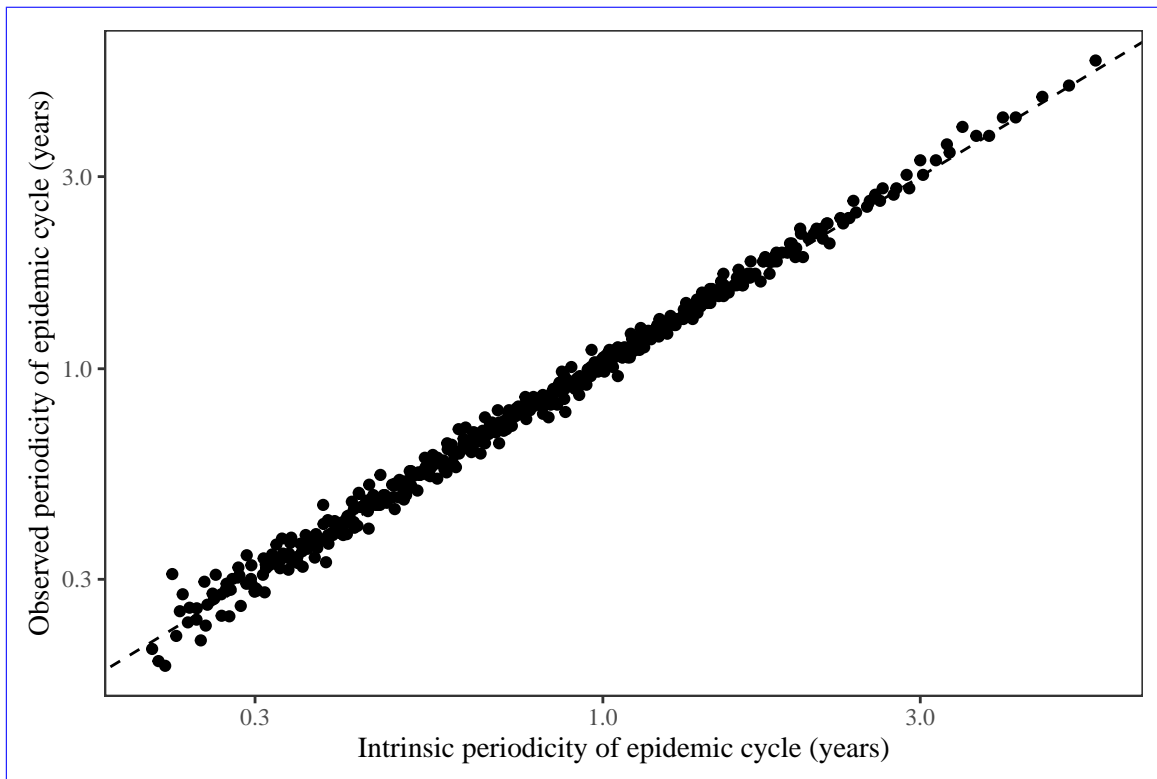


Figure S13: **Comparison of resilience estimates.** Each point represents a resilience estimate for a specific pathogen. Comparison between the observed and intrinsic periodicity of the epidemic cycle of the seasonally unforced SIRS model. The observed periodicity of the epidemic corresponds to the periodicity at a specific country which maximum spectral density occurs. The x values represent intrinsic periodicity of the original resilience estimates presented in Figure 4. The y values represent epidemic corresponds to $2\pi/\text{Im}(\lambda)$, where $\text{Im}(\lambda)$ is the original resilience estimates presented in Supplementary Figure S14 imaginary part of the eigenvalue.

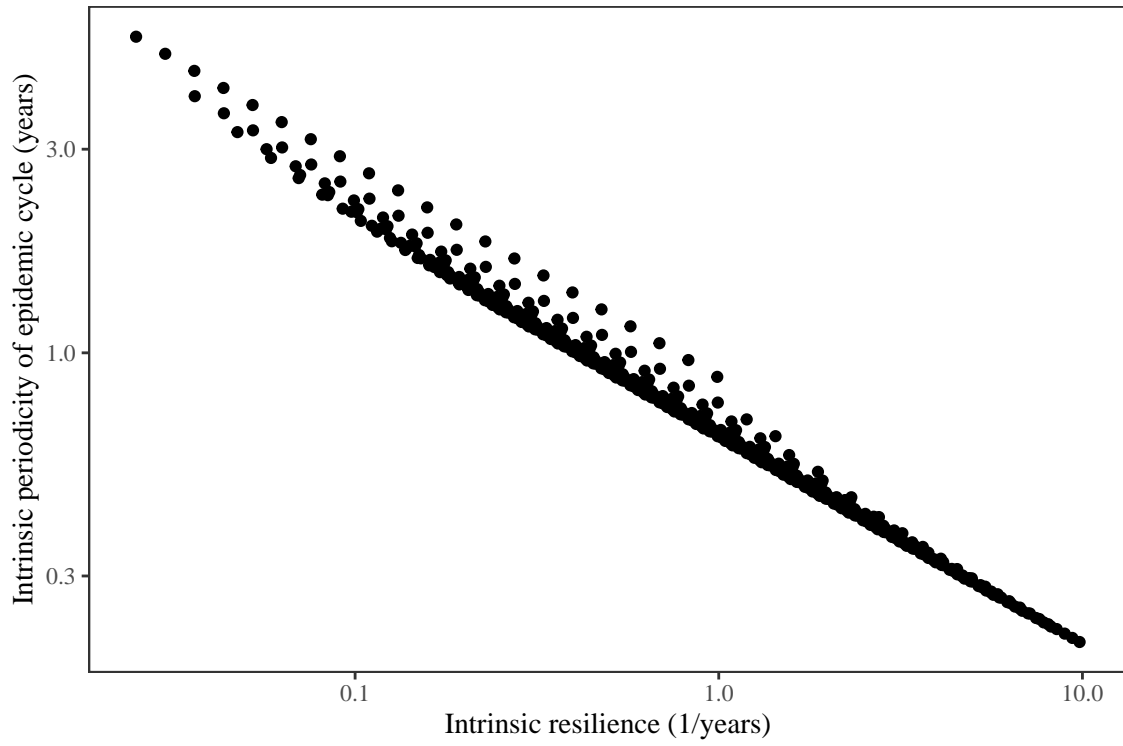


Figure S14: [Comparison between the intrinsic resilience and periodicity of the epidemic cycle of the seasonally unforced SIRS model.](#) The intrinsic resilience of the epidemic corresponds to the negative of the real value of the eigenvalue $-Re(\lambda)$. The intrinsic periodicity of the epidemic corresponds to $2\pi/Im(\lambda)$, where $Im(\lambda)$ is the imaginary part of the eigenvalue.

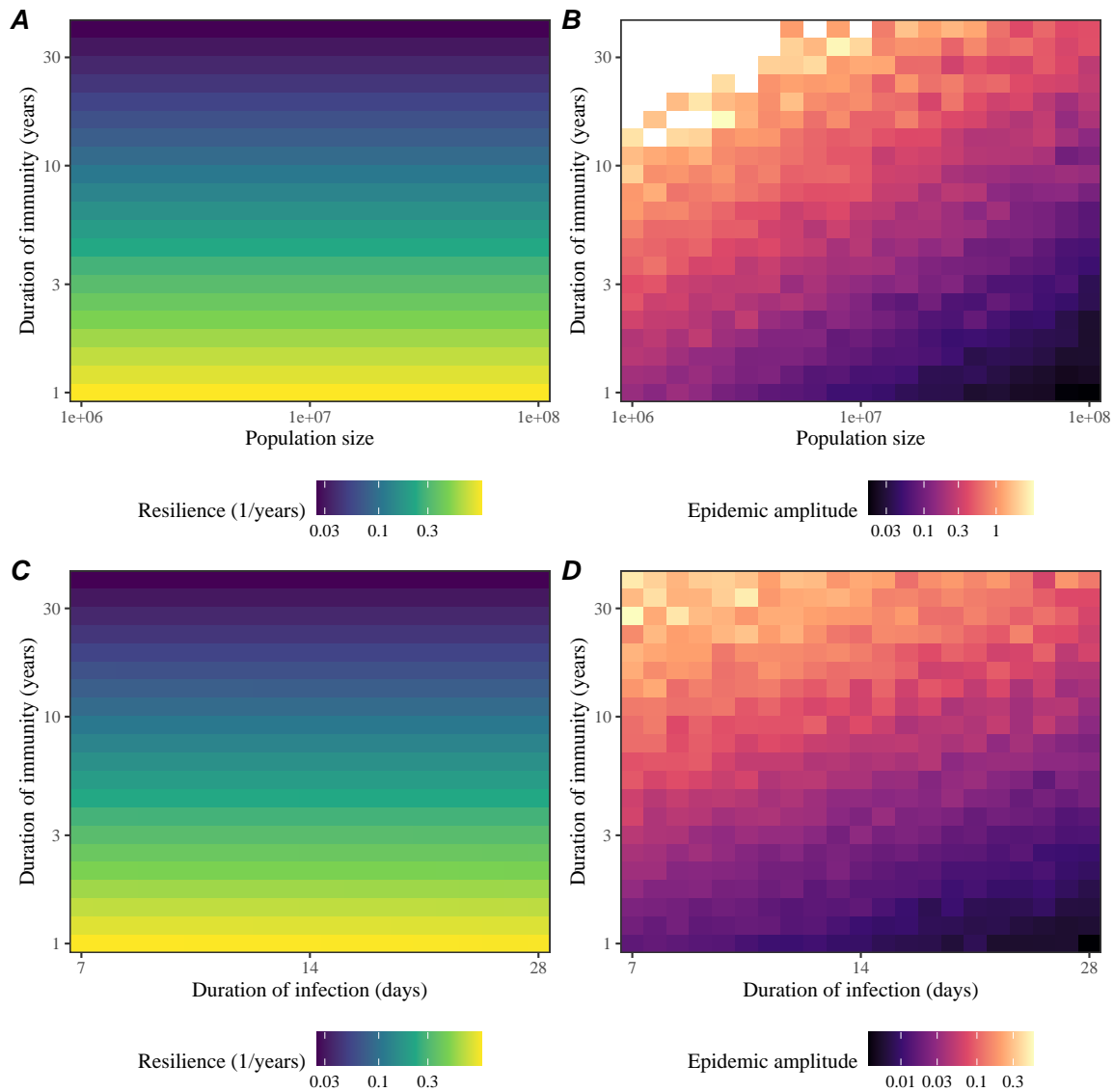


Figure S15: **Impact of population size and the average duration of infection of a host-pathogen system on its sensitivity to stochastic perturbations.** (A) Intrinsic resilience of a system as a function of population size and the average duration of immunity. (B) Epidemic amplitude as a function of population size and the average duration of immunity. (C) Intrinsic resilience of a system as a function of the average duration of infection and immunity. (D) Epidemic amplitude as a function of the average duration of infection and immunity. The epidemic amplitude corresponds to $(\max I - \min I)/(2\bar{I})$, where \bar{I} represents the mean prevalence.

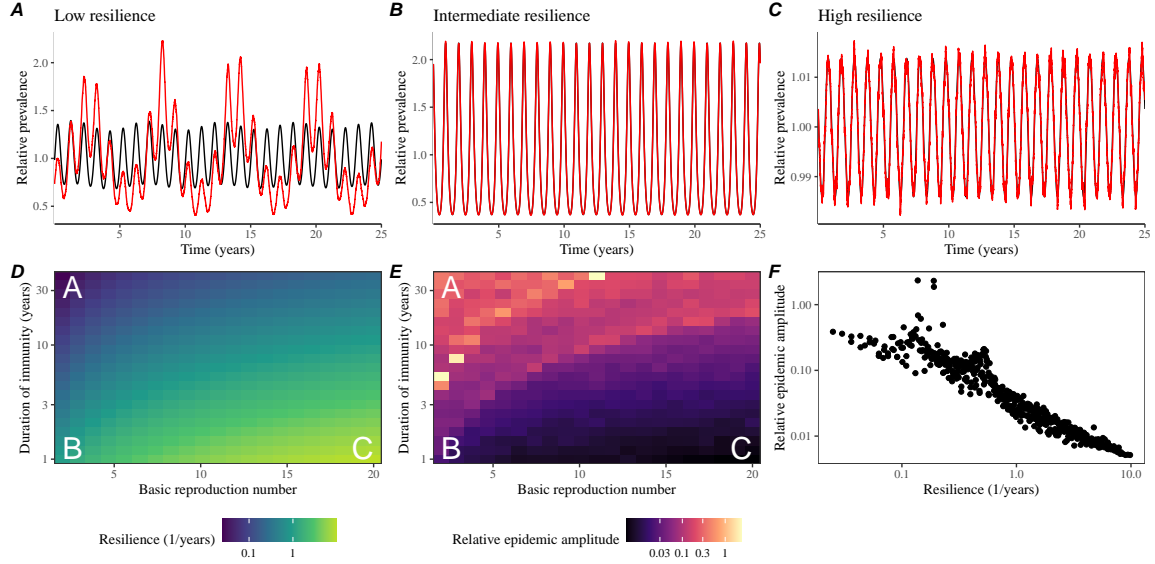


Figure S16: **Linking resilience of a host-pathogen system to its sensitivity to stochastic perturbations for the seasonally forced SIRS model.** (A–C) Epidemic trajectories of a stochastic SIRS model with demographic stochasticity across three different resilience values: low, intermediate, and high. The relative prevalence was calculated by dividing infection prevalence by its mean value. Black lines represent deterministic epidemic trajectories. Red lines represent stochastic epidemic trajectories. (D) The intrinsic resilience of the seasonally unforced system as a function of the basic reproduction number \mathcal{R}_0 and the duration of immunity. (E) The relative epidemic amplitude, a measure of sensitivity to stochastic perturbations, as a function of the basic reproduction number \mathcal{R}_0 and the duration of immunity. To calculate the relative epidemic amplitude, we first take the relative difference in infection prevalence between stochastic and deterministic trajectories: $\epsilon = (I_{\text{stoch}} - I_{\text{det}})/I_{\text{det}}$. Then, we calculate the difference between maximum and minimum of the relative difference and divide by half: $(\max \epsilon - \min \epsilon)/2$. Labels A–C in panels D and E correspond to scenarios shown in panels A–C. (F) The relationship between pathogen resilience and relative epidemic amplitude.

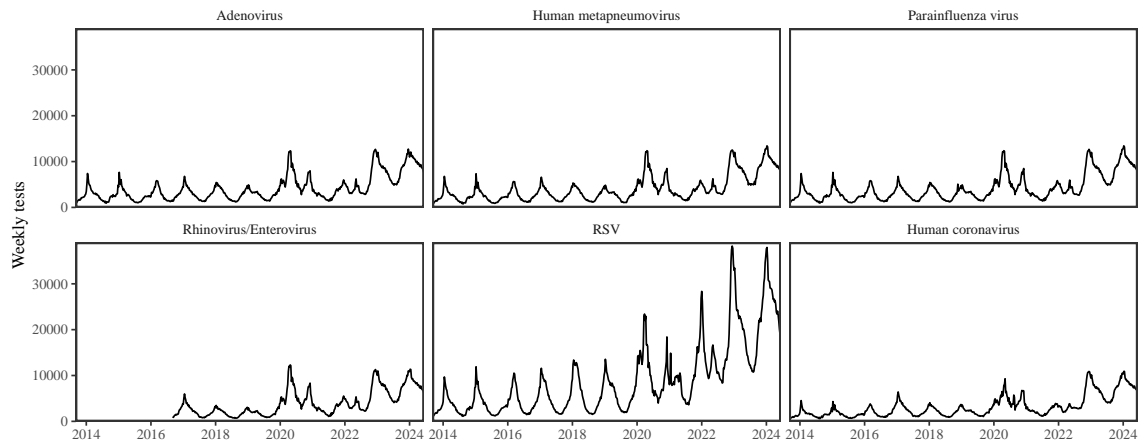


Figure S17: **Testing patterns for respiratory pathogens in Canada.**

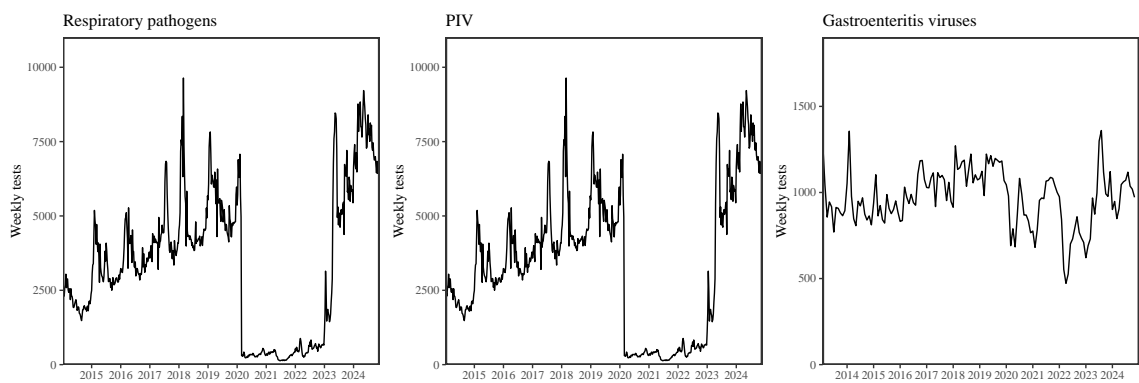


Figure S18: **Testing patterns for respiratory pathogens, PIV, and gastroenteritis viruses in Hong Kong.**

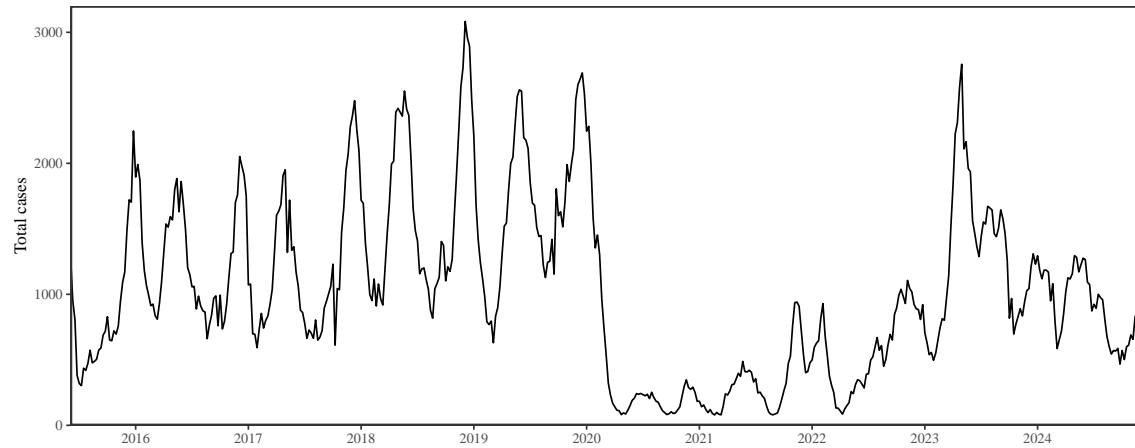


Figure S19: Total number of reported respiratory infection cases in Korea.

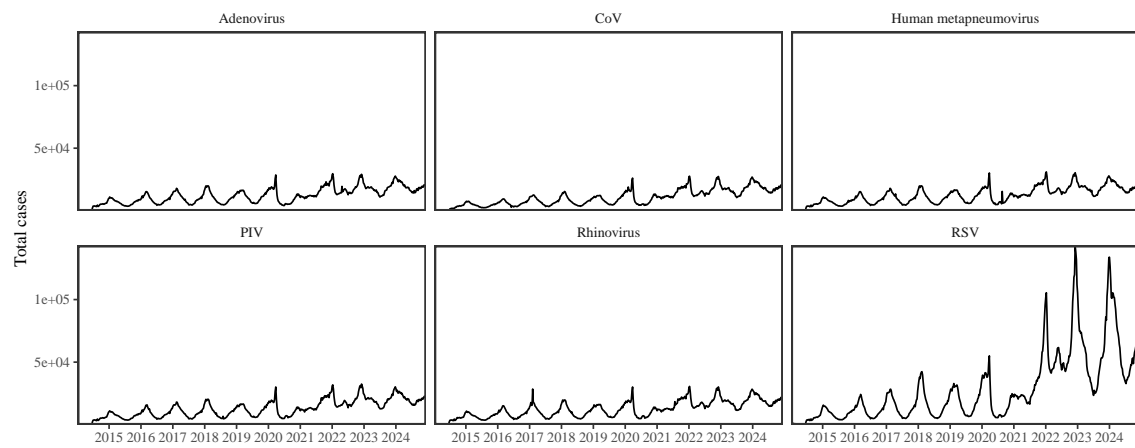


Figure S20: Testing patterns for respiratory pathogens in the US reported through the NREVSS.